Supporting Information

Construction and Validation of Nano Gold Tripods for Molecular Imaging of Living Subjects

Kai Cheng[1,2,3], Sri-Rajasekhar Kothapalli[1, 3], Hongguang Liu[1,2,3], Ai Leen Koh[4], Jesse V. Jokerst[1, 3], Han Jiang[1,2,3], Meng Yang[1,2,3], Jinbo Li[1,2,3], Jelena Levi[1,2,3], Joseph C. Wu[1, 3], Sanjiv S. Gambhir[1,2,3], Zhen Cheng[1,2,3,]*

[1]Molecular Imaging Program at Stanford (MIPS), [2]Canary Center at Stanford for Cancer Early Detection, [3]Department of Radiology and Bio-X Program, School of Medicine, [4]Stanford Nanocharacterization Laboratory, Stanford University, 1201 Welch Road, Lucas P095, Stanford, CA 94305-5484, USA

KEYWORDS: gold tripods, positron emission tomography, photoacoustic imaging

Index of Content

A. Supplementary Materials **4**

2. Branched Au NPs (Au-Pt NPs, Au-dipods, Au-tripods and Au-tetrapods) 5
3. Syntheses of functional polyethylene glycols (PEG) 6
4. PEGylation of Au-tripods 10
5. Conjugation of Au-tripods with cRGD (RGD-Au-tripods) 11
6. Synthesis and surface modification of gold nanorods 11
7. ^{64}Cu labeling of NPs. 12
8. Cell Culture and Animal Models. 13

B. Characterizations and Methods **14**

1. Microscopy 14
2. Particle Size and Zeta Potential 15
3. Numerical analysis of the optical properties of Au-tripods and Au-rods 16
4. Cell viability test 16
5. Inductively Coupled Plasma Mass Spectrometry (ICP-MS) 17
6. Histology and Silver Enhancement 18
7. MicroPET Imaging 18
8. Biodistribution 19
9. Spectral Measurements 20
10. Photoacoustic Imaging (PAI) 20
11. Photoacoustic signal linearity characterization of Au-tripods and Au-rods 21
12. *In vitro* targeting of RGD-Au-tripods (PAI and ICP). 22
13. Limit of Detection for Tripod-targeted U87MG cells 23
14. Photoacoustic detection of Au-tripods in living mice. 24
15. RGD-Au-tripod tumor targeting in living mice. 24
16. Pathologic Evaluation 25

C. Supplementary Data and Discussion **26**

1. Characterization of Nanoparticles 26

    1.1. Particle size of cubic Pt NPs 26
    1.2. Synthesis and Characterization of Branched Au-nanostructures 28
  2. Characterization of Gold Nanorods 36
  3. Determination of concentrations of tripods and rods 37
  4. Optical properties and simulation 38
  5. PEGylation of Au-tripods 45
    5.1. PEG coating 45
    5.2. Quantification of PEG density on PEGylated Au-tripods. 47
  6. Size, Zeta Potential and stability test of functionalized Au-tripods. 49
  7. Quantification Analysis of number of NOTA groups on NOTA- RGD-Au-tripods. 51
  8. Cellular internalization of RGD-Au-tripods. 52
  9. Radio labeling and *in vivo* biodistribution and tumor targeting of Au-tripods 54
  10. Pilot acute toxicity analysis of tripods 59
  11. in vitro and in vivo PAI 63
  12. Histologic and microscopic examination 65
References for Supporting Information 67

A. Supplementary Materials

The integrin $\alpha_v\beta_3$ targeting peptide cyclo (Arg-Gly-Asp-D-Phe-Cys) (cRGDfC) was ordered from Peptides International, Inc (Louisville, KY). The p-SCN-Bn-NOTA was purchased from Macrocyclics, Inc. Hydrogen tetrachloroaurate (III) hydrate ($HAuCl_4$) and platinum (II) acetylacetonate ($Pt(acac)_2$) was ordered from Strem Chemicals, Inc. *N*-hydroxysuccinimide (NHS), *N*-hydroxysulfosuccinimide (sulfo-NHS), succinimidyl 4-(*N*-maleimidomethyl) cyclohexane-1-carboxylate (sulfo-SMCC), and 1-ethyl-3-(3-dimethylaminopropyl) carbodiimide, hydrochloride (EDC) were purchased from Thermo Fisher Scientific. Hexadecyltrimethylammonium bromide (CTAB) was ordered from Sigma-Aldrich. All other chemicals were purchased from Sigma-Aldrich. Triethylamine and dichloromethane (DCM) were distilled prior to use, and *N, N'*-dimethylformamide (DMF) was stored over molecular sieves. Other solvents and chemicals were used as received. All buffers and media were purchased from Invitrogen Corp. Deionized water was obtained from a Millipore Milli-DI Water Purification system. The dialysis membrane tubing (MWCO: 12,000 ~ 14,000, and 100,000) were purchased from Spectrum laboratories.

1. Size tuning of cubic Pt NPs

The size of various cubic Pt NPs was successfully tuned by adjusting the reaction conditions in a precise manner. Truncated-cubic Pt NPs (5 nm) were prepared by the modified procedure here. The platinum precursor (platinum (II) acetylacetonate, or Pt $(acac)_2$, 100 mg, 0.25 mmol) was dispersed in 10 ml of octadecene (ODE) containing 1 ml of oleic acid and 1 ml of oleylamine with stirring under nitrogen protection. The resultant mixture was preheated to 70°C until the platinum salt was dissolved and the solution turned bright yellow. The mixture was then heated up to 140°C for 2 min. Iron precursor (iron pentacarbonyl, $Fe(CO)_5$, 0.01 ml in 0.1 ml of hexane (0.742M), 0.0742 mmol) in hexane was quickly injected in the above solution. The resultant mixture was heated up to 200 °C at a heating rate of 5°C/min and then kept at this temperature for 1 hour before it was cooled down to room temperature by removing the heating mental. The particles were precipitated out by adding 70 ml of isopropanol and collected by using a high-speed centrifuge (7000 rtf, 8 min). The resultant particles were re-dispersed in 5 ml of hexane and then precipitated out by adding ethanol. This purification step was repeated twice to remove the extra surfactant and ODE. The final product (5 nm cubic Pt NPs) was dispersed in 10 ml of hexane in the presence of 0.01 ml of oleylamine for further use. Truncated-cubic Pt NPs (6 nm) were prepared according to the similar procedure described above, except for the injection temperature of iron precursor (i.e. 120°C).

Truncated-cubic Pt NPs (7 and 8 nm) were synthesized by a seed-mediated procedure here. Truncated-cubic Pt NPs with the sizes of either 5 or 6 nm prepared freshly were used as seeds for the syntheses of 7 and 8 nm truncated-cubic Pt NPs, respectively. Generally, the solution of platinum precursor was prepared according to the same procedure of the synthesis of 5 and 6 nm Pt NPs described in the previously section. Once Pt precursor was completely dissolved at 70°C, the mixture was continuously heated to 120°C. Forty milligram of 5 nm Pt NPs (dispersed in 2 ml hexane) was quickly injected in the above mixture. After 2 min of stirring, iron precursor (iron pentacarbonyl, $Fe(CO)_5$, 0.01 ml in 0.1 ml of hexane (0.742M), 0.0742 mmol) in hexane was quickly injected in the hot solution. The resultant solution was heated to 200 °C at a heating rate of 5°C/min and then kept at this temperature for 1 hour before it was cooled down to room temperature. The particles were precipitated out by adding 70 ml of isopropanol and collected by a centrifuge (7000 rpm, 8 min). The resultant particles were re-dispersed in 5 ml of hexane and then precipitated out by adding ethanol. This purification step was repeated twice to remove the extra surfactant and ODE. The final product (7 nm truncated-cubic Pt NPs) was dispersed in 10 ml of hexane in the presence of 0.01 ml of oleylamine for further use. The truncated-cubic Pt NPs with the size of 8 nm were obtained by the same procedure, but with 5 nm Pt NPs as seeds.

2. Branched Au NPs (Au-Pt NPs, Au-dipods, Au-tripods and Au-tetrapods)

2.1. Synthesis of Au-Tripods. The gold precursor (hydrogen tetrachloroaurate, $HAuCl_4$, 100 mg, 0.29 mmol) was dissolved in 20 ml of ODE containing 2 ml of oleylamine under nitrogen protection. After stirred at room temperature for 5 min, the solution was heated up to 80°C. Twenty milligram of 6.5 nm freshly synthesized Pt NPs (dispersed in 1 ml of hexane) was quickly injected in the above solution. The resultant mixture was then heated up to 110°C for and kept at this temperature for one hour before it was cooled down to room temperature. The solution finally turned to gray-purplish color, indicating the formation of gold branched nanostructures. The particles were precipitated out by adding 30 ml of isopropanol and collected by a centrifuge (3000 rcf, 5 min). The resultant particles were re-dispersed in 5 ml of hexane and then precipitated out by adding ethanol. This purification step was repeated twice to remove the extra surfactant and ODE. The final product (Au-tripods) was dispersed in 10 ml of hexane in the presence of 0.01 ml of oleylamine for further use.

2.2. Synthesis of Au-Pt NPs. The Au-Pt NPs were obtained by the similar recipe described in the previous section while 5 nm Pt NPs were used as seeds.

2.3. Synthesis of Au-dipods. The Au-dipods were obtained by the similar recipe described in the previous section while 6 nm Pt NPs were used as seeds.

2.4. Synthesis of Au-tetrapods. The Au-tetrapods were obtained by the similar recipe described in the previous section while 8 nm Pt NPs were used as seeds.

3. Syntheses of functional polyethylene glycols (PEG)

3.1. Synthesis of lipoate NHS Ester (LP-NHS):

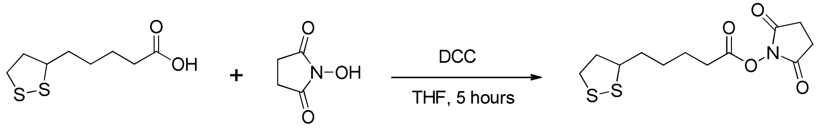

The LP-NHS was synthesized according to the literature.[1] Basically, to a solution of lipoic acid (2.06 g, 10 mmol) and and *N*-hydroxysuccinimide (NHS, 1.2 eq. 12 mmol, 1.381 g) in 100 ml of dry tetrahydrofuran at 4°C was added slowly a solution of dicyclohexylcarbodiimide (1.2 eq. 12 mmol, 2.476 g, solubility: 0.1 g/ml in CH_2Cl_2) in 10 ml of tetrahydrofuran. The mixture was warmed to room temperature and stirred for 5 h. The precipitate was removed by vacuum filtration and the solvent evaporated in vacuum. The crude product was redissolved in 100 ml of ethyl acetate and filtered once more by vacuum filtration. The product was recrystallized from a solution of hot ethyl acetate/hexane (1:1, v/v) as a pale-yellow solid (Yield = 75.8%). 1H NMR (400 MHz, $CDCl_3$): δ (ppm) 3.583 (m, 1H), 3.154 (m, 2H), 2.839 (s, 4H), 2.630 (t, 2H), 2.472 (m, 1H), 1.93-1.56 (7H). 13C NMR (125 MHz, CDCl3): δ (ppm) 169.31, 168.87, 56.29, 40.34, 38.71, 34.61, 30.98, 28.50, 25.79, 24.56.

3.2. Synthesis of polyethylene glycol bisamine (PEG-x-diamine, x = 1000, 2000, 3400 or 6000 g/mol). PEG-x-diamine was synthesized according to the literature.[2]

3.2.1. Synthesis of polyethylene glycol dichloride (PEG-x-Cl, x = 1000, 2000, 3400 or 6000). Polyethylene glycol (PEG-x-OH, 2 mmol, 4 mmol of OH) was dissolved in 50~150 ml of dry toluene and dried by azeotropic distillation. After dry pyridine (4 mmol, 322 μl) was added, thionyl chloride (4 mmol, 0.29 ml) was added dropwise during 30 min under reflux. The mixture was heated for 4 hr before it was cooled to room temperature. The resultant mixture was filtered from pyridine hydrochloride and the toluene was evaporated in vacuum. The residue was dissolved in dichloromethane (DCM), dried over anhydrous K_2CO_3 and filtered. The filtrate was precipitated by cold ether. The final product PEG-x-Cl was obtained by recrystallization in DCM/ethyl ether.

3.2.2. Synthesis of polyethylene glycol diazide (PEG-x-N_3, x = 1000, 2000, 3400 or 6000). Sodium azide (40 mmol, 2.6 g) was added to a solution of PEG-3400-Cl (2 mmol, 6.8 g) in 60 ml of dry DMF. The mixture was stirred at 120°C for 2 hrs. The resultant mixture was cooled, filtered and the DMF was evaporated in vacuum. The residue was taken up in DCM, cooled, filtered and dried over anhydrous K_2CO_3 and filtered. The final product PEG-3400-N_3 was obtained by recrystallization in DCM/ethyl ether.

3.2.3. Synthesis of polyethylene glycol bisamine (PEG-x-NH2, x = 1000, 2000, 3400 or 6000). The PEG-x-N_3 (2 mmol) was dissolved in 60 ~ 120 mL of dry tetrahydrofuran (THF), and triphenylphosphine (2.2 eq. 4.4 mmol, 1.15 g) was added. The solution was stirred at room temperature for 4 hours before adding 1 ml of water. The resultant solution was stirred overnight. The THF was removed in vacuum, and 20 ml of water was added. The precipitate was removed by vacuum filtration and the filtrate washed with toluene (3×10 ml). The water was removed in vacuo and residue was dissolved in DCM and dried over anhydrous K_2CO_3 and filtered. The pure product as light-yellow powder was obtained by recrystallization in DCM/ethyl ether.

3.3. Synthesis of *O*-(3-aminopropyl) polyethylene glycol lipoate amide (LP-PEG-x-NH2, x = 2000, 3400 or 6000). To a stirred solution of the PEG-x-bisamine (PEG-x-NH2, x = 1000, 2000, 3400 or 6000, 0.2 mmol) and triethylamine (20 mg, 0.2 mmol) in 10 ml of 1,4-dioxane was added dropwise a solution of LP-NHS (0.8 eq. 0.16 mmol) in 2 mL of 1,4-dioxane over 1 h. The reaction mixture was allowed to stand overnight until thin layer chromatography (TLC) analysis showed no lipoate-NHS ester remaining. After the solvent was evaporated, the crude product was purified by basic alumina column (dichloromethane/methanol, 95:5). The resultant product was recrystallized from a solution of DCM/ethyl ether as a white solid (yield = 60%).

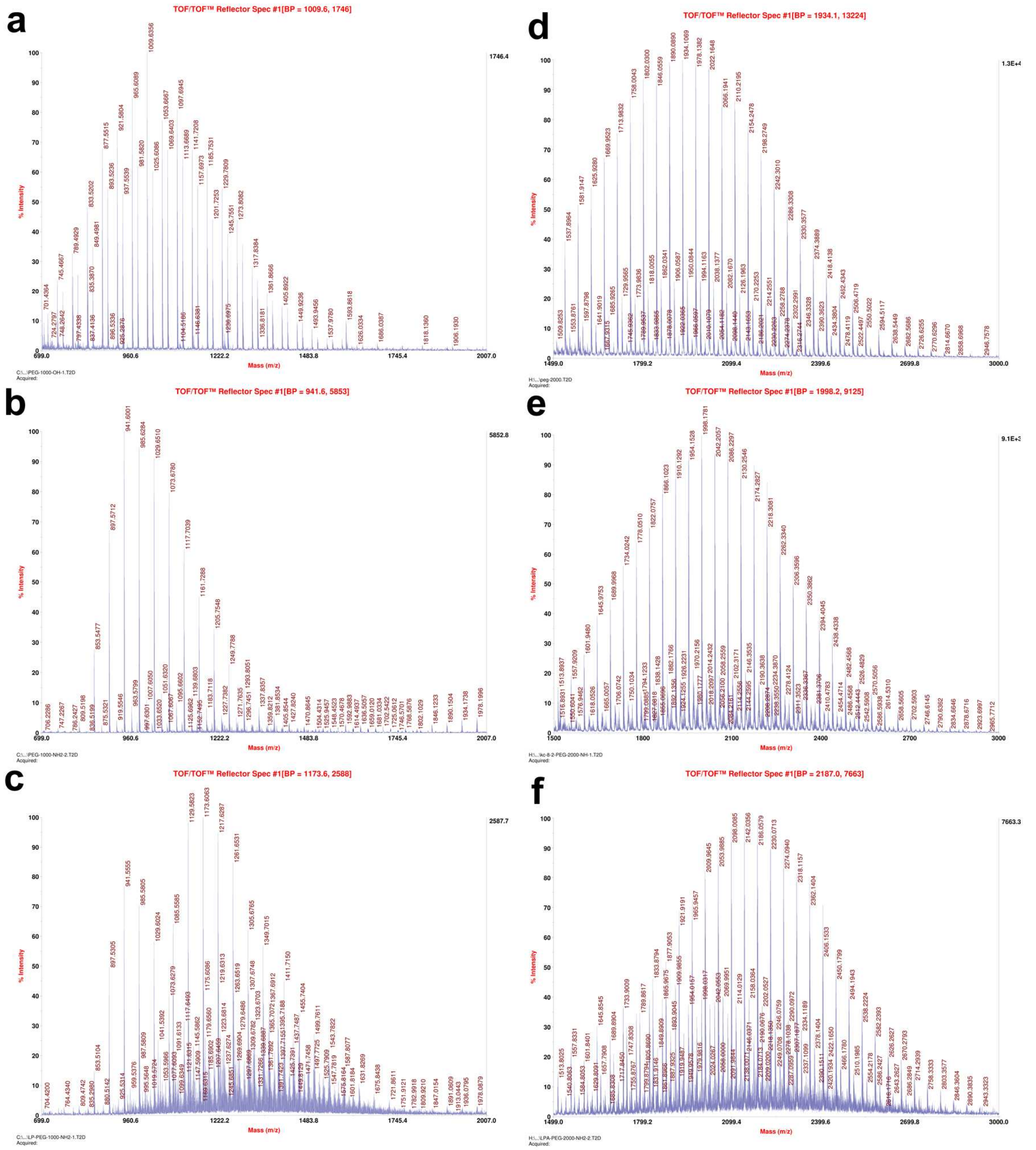

Figure S1. MALDI Mass spectra of (**a**) PEG-1000-OH ([PEG-1000 + H]$^+$), (**b**) PEG-1000-NH2 ([PEG-1000-NH2 + H]$^+$), (**c**) LP-PEG-1000-NH2 ([LP-PEG-1000-NH2 + H]$^+$), (**d**) PEG-2000-OH ([PEG-2000 + H]$^+$), (**e**) PEG-2000-NH2 ([PEG-2000-NH2 + H]$^+$), (**f**) LP-PEG-2000-NH2 ([LP-PEG-2000-NH2 + H]$^+$).

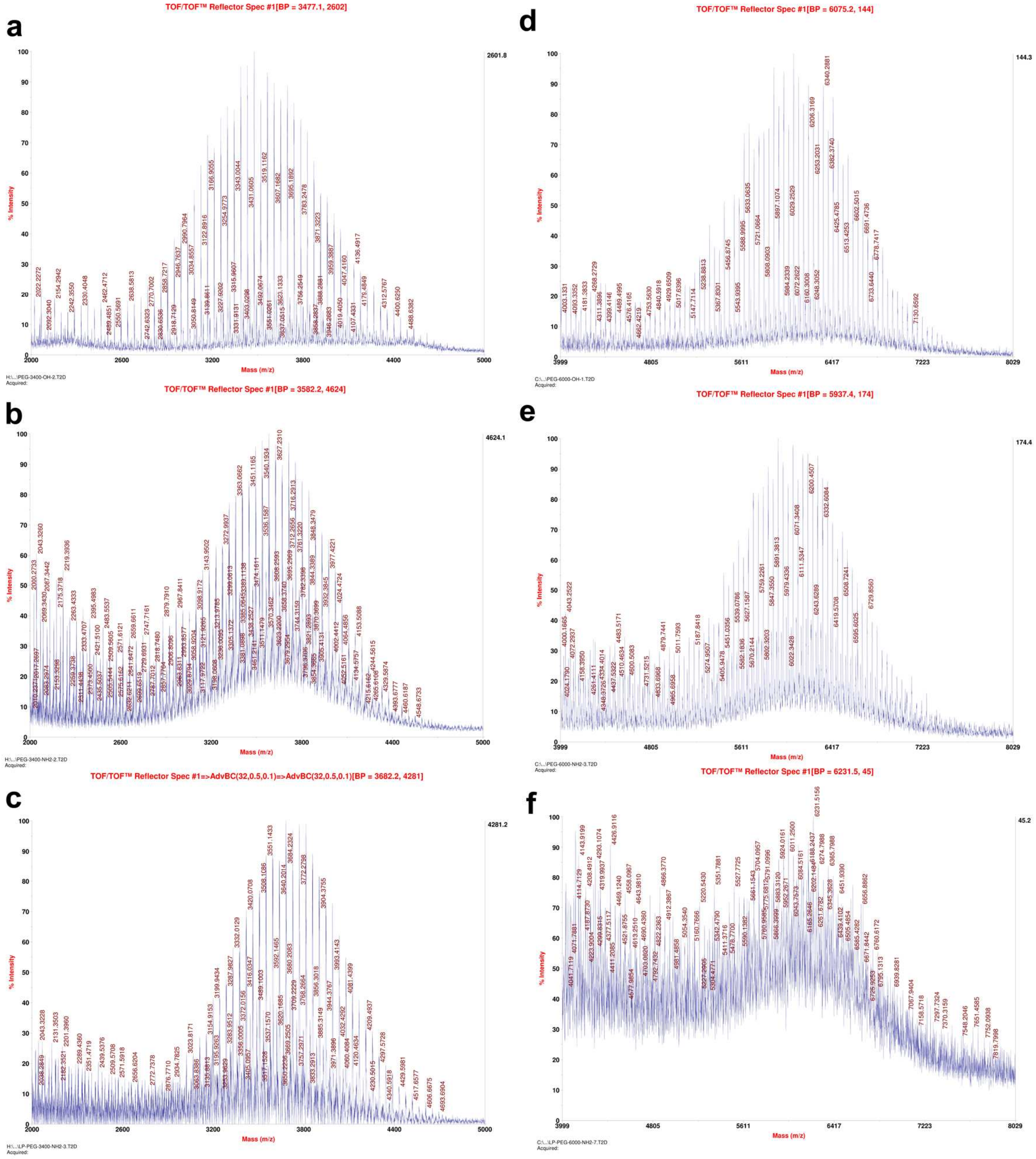

Figure S1-continued. MALDI Mass spectra of (**a**) PEG-3400-OH ([PEG-3400 + Na]$^+$), (**b**) PEG-3400-NH2 ([PEG-3400-NH2 + H]$^+$), (**c**) LP-PEG-3400-NH2 ([LP-PEG-3400-NH2 + H]$^+$). (**d**) PEG-6000-OH ([PEG-6000 + Na]$^+$), (**e**) PEG-6000-NH2 ([PEG-6000-NH2 + Na]$^+$), (**f**) LP-PEG-6000-NH2 ([LP-PEG-6000-NH2 + H]$^+$).

4. PEGylation of Au-tripods

The Au-tripods (10 mg, sample weight after dried under nitrogen) were dissolved in 2 ml of chloroform with stirring. The solution of LP-PEG-x-NH2 (0.02 mmol, x = 2000, 3400 or 6000, when x = 3400, weight = 72 mg) in 1 ml of chloroform was added into the above NP solution. The mixture was stirred at room temperature for 24 hours. PEGylated Au-tripods were precipitated by adding 20 ml of hexane, collected by a brief centrifugation, and dried under the nitrogen gas flow. The PEGylated Au-tripods were then dispersed in water. The unbound PEG and any other excess reagents were removed by dialysis against water or phosphate-buffered saline (PBS) (10 mM, pH 7.4) by tubing (Spectrum Spectra/Por dialysis membrane tubing, MWCO = 12 kDa). Any impurity or precipitate was removed by a 0.22 μm syringe filter. The final gold or platinum concentration of PEGylated Au-tripods was measured by Inductively coupled plasma mass spectrometry (ICP-MS) analysis. The same PEGylation process made Au-Pt NPs, Au-dipods, and Au-tetrapods water-soluble. Those NPs were characterized with transmission electron microscopy (TEM), UV-vis absorption spectroscopy, and dynamic light scattering (DLS).

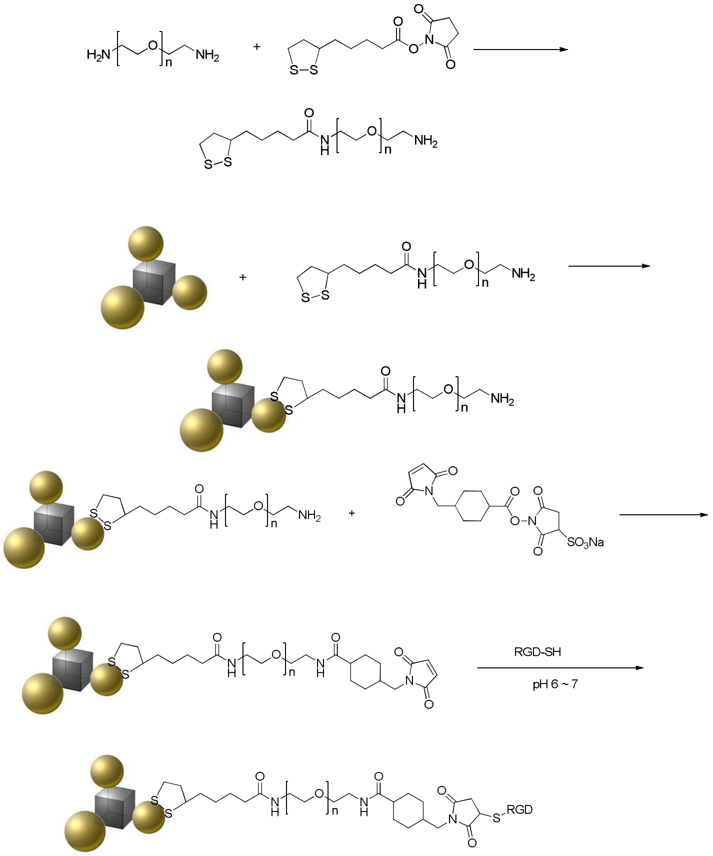

Scheme S1. Illustration of synthesis of water-soluble Au-tripods and synthesis of RGD-Au-tripods.

5. Conjugation of Au-tripods with cRGD (RGD-Au-tripods)

The crosslinker solution was prepared freshly. The sulfo-SMCC (0.5 mg, 1.5 μmol) was first dissolved in 15 μl of DMSO. The water-soluble Au-tripods (Au-tripod-PEG-x-NH2 (x = 2000, 3400, or 6000), 100 nM, 0.5 ml, 5×10^{-11} mol, see the determination of concentrations of tripods and rods) in 10 mM PBS (pH = 7.2) were incubated with the above crosslinker solution for 2 hours at room temperature. The resultant thiol-active Au-tripods ran through a PD-10 column (GE Healthcare, Piscataway, NJ) pre-washed with 10 mM PBS (pH = 7.2) to remove excessive sulfo-SMCC and by-products. The purified Au-tripods were concentrated to the final volume of 0.5 ml with a centrifugal-filter (Amicon centrifugal filter device, MWCO = 30 kDa). The cRGDfC stock solution (50 μl of 5 mM in the degassed water, 0.25 μmol) was added to the above NP solution with stirring. The final RGD concentration in the mixture was 0.5 mM. The conjugation reaction proceeded for 24 hours at 4°C. The uncoupled RGD and byproducts were removed through PD-10 column. The resultant product, RGD-Au-tripods, was concentrated by a centrifugal-filter (Amicon centrifugal filter device, MWCO = 30 kDa) and stored at 4°C for one month without losing targeting activity. The final RGD-Au-tripods was reconstituted in PBS and filtered through a 0.22 μm filter for cell and animal experiments. The gold and platinum concentrations of RGD-Au-tripods were measured by ICP-MS analysis.

The process to conjugate the tripods with both RGD and NOTA was similar to the conjugation of tripods and RGD, except that sulfo-SMCC solution was mixed with NOTA aqueous solution in the first step before added into the tripod solution. Briefly, The sulfo-SMCC (0.5 mg, 1.5 μmol) was dissolved in 15 μl of DMSO and mixed with 4.5 μl of p-SCN-Bn-NOTA solution in the water (33 mM, 0.15 μmol). The ratio of SMCC to NOTA was optimized according to the specific activity of radioactive tracer labeled NPs.

6. Synthesis and surface modification of gold nanorods

Synthesis of gold nanorods. The gold nanorods were prepared by the seeded growth method according to procedure described in the literature with slight modifications.[3] Briefly, gold seeds were prepared by mixing 5 ml of 0.2 M CTAB with 5 ml of 0.5 mM gold precursor ($HAuCl_4$) with vigorous stirring. To the stirred mixture, 0.6 ml of ice-cold 10 mM sodium borohydride ($NaBH_4$) was quickly added. The resultant mixture was shaken for 2 min and then kept at 25°C for the next step. The growth solution was prepared by the following recipe: 50 ml of 1 mM $HAuCl_4$ solution was added to the mixture of 50 ml of 0.2 M CTAB and 2.0 ml of 4 mM silver nitrate ($AgNO_3$) solution at 25°C. The color of mixture changed from dark yellow to colorless after addition of 0.7 ml of 78.8 mM ascorbic acid. Finally, 120 µl of seed solution was added to the growth solution at 27~30°C. The solution became brownish color over 20 min. The gold nanorods (54 nm in length × 18 nm in diameter, aspect ratio = 3) were collected with three rounds of centrifugation at 14000 rcf for 20 min and washed with water.

PEGylated gold nanorods. The as-synthesized gold nanorods initially stabilized with CTAB were functionalized with disulfide-terminated PEG linkers (LP-PEG-3400-NH2) via the ligand exchanging process. To a solution of gold nanorods (0.5 ml, 1 mg Au/ml, 6.26 nM in water, see the determination of concentrations of tripods and rods) was added 100 µl of 40 mM LP-PEG-3400-NH2 (4 µmol). The mixture was stirred for 24 hours at room temperature, and was then dialyzed against water for 48 hours with dialysis tubing (Spectrum Spectra/Por dialysis membrane tubing, MWCO = 12 kDa).

Surface modification of PEGylated gold nanorods. The process to conjugate the gold nanorods with either RGD alone, or both RGD and NOTA, was as same as the procedure of the RGD-Au-tripods or NOTA-RGD-tripods described in previous section. The final product was reconstituted in PBS and filtered through a 0.22 µm filter for cell and animal experiments. Those functional gold nanorods were characterized with TEM, UV-vis absorption spectroscopy, and DLS.

7. ^{64}Cu labeling of NPs.

The ^{64}Cu labeling procedure was conducted according to the methods previously described.[4] Briefly, the stock solution of $^{64}CuCl_2$ (supplied by the University of Wisconsin-Madison) was diluted with 200 µl of 0.1 M sodium acetate buffer (pH = 6.0). One mCi of 64Cu stock solution (37 MBq) was then added to 300 µL of NOTA-RGD-Au-tripods (~100 nM, 30 pmol, 0.3 mg of [Au+Pt], see the determination of concentrations of tripods and rods) buffered in 0.1 M sodium acetate buffer (pH = 6.0). After the resultant solution was incubated for 1 hour at 40°C, the radiolabeled NPs were applied to a PD-10 column and eluted with PBS to remove excess ^{64}Cu. The radioactive fractions containing ^{64}Cu-NOTA-RGD-Au-tripods were collected and the radio-labeling yield was generally 60~70%. The purification of radio-labeling solution using a PD-10 column afforded ^{64}Cu-NOTA-RGD-Au-tripods with a modest specific activity (0.59~0.74 MBq/pmol particle, see the concentration conversion in Supporting

Information Section C.4). A CRC-15R PET dose calibrator (Capintec Inc., Ramsey, NJ) was used for all radioactivity measurements.

The procedure of ^{64}Cu labeling of either NOTA-Au-tripods or NOTA-RGD-Au-rods was as same as that of NOTA-RGD-Au-tripods. In the case of ^{64}Cu labeling of RGD-Au-rods, the same weight of NOTA-RGD-Au-rods in 300 μl of 0.1 M sodium acetate buffer (pH = 6.0) was incubated with 1 mCi of ^{64}Cu stock solution (37 MBq) for 1 hour at 40°C, followed by the purification of the radio-labeling solution using a size-exclusion column. The radio-labeling yield was generally 60~70%. The specific activity of gold nanorods (~740 MBq/nmol particle) was ten-times higher than that of gold tripods. The characterization of radio-labeled NPs was performed after the complete decay of the radioactive source.

Serum Stability Test of radio-label ^{64}Cu on Au-tripods. The ^{64}Cu-NOTA-RGD-Au-tripods (100 μCi, 3.7 MBq) was incubated in the mouse serum at 37°C for 24 hours. Aliquots of tripod solution in the serum were collected at certain time points and filtered through spin filters (100 kDa cutoff). The radio activities of the filtrates were measured over time to confirm the stability of radio-chelating reagents on the tripods.

8. Cell Culture and Animal Models.

The U87MG human glioblastoma cell line obtained from American Type Culture Collection was cultured under standard condition. All animal experiments were conducted in accordance with the Administrative Panel on Laboratory Animal Care at Stanford University, and were within the guidelines of humane care of laboratory animals. Female nu/nu nude mice (6~8 weeks, Charles River Laboratories) were used for in vivo targeting studies. The U87MG xenograft tumor models were prepared by subcutaneous implantation of 5×10^6 cells in 100 μl PBS into either the right front flank or the right hind flank of female nu/nu nude mice for PET imaging or PA imaging, respectively. The mice were subjected to small-animal PET and PAI studies when the tumor volume reached 200~400 mm^3 (3~4 weeks after inoculation). Tumor-bearing mice were randomized before being used in either small animal PET imaging, PA imaging, or the biodistribution study. Various functional Au-tripods or Au-rods was administered to the mice in PBS by intravenous injection of 100 ~200 μl into the tail vein. Mice were euthanized by CO_2 asphyxiation. Tissues or organs harvested for analysis were rinsed with PBS and blotted dry on clean filter paper.

B. Characterizations and Methods

1. Microscopy

The high-resolution transmission electron microscope (HRTEM) and scanning transmission electron microscope (STEM) images were recorded with a spherical aberration (imaged) corrected FEI Titan 80-300 environmental (Scanning) transmission electron microscope operated at 300 kV. The regular TEM images were recorded with a FEI Tecnai G2 F20 X-TWIN transmission electron microscope operated at 200 kV. Samples were deposited and dried on copper grids covered with a Formvar/carbon support film, followed by plasma cleaning. Electron energy-loss spectroscopy (EELS) were performed in scanning, monochromated mode using the FEI Titan 80-300 environmental (S)TEM operated at 300 kV, which is equipped with a Gatan 866 Tridiem EEL spectrometer. A 50 micrometer C3 aperture, camera length of 48 mm, entrance aperture of 2.5 mm and dispersion of 0.01 eV per channel were used for the EEL spectra acquisition. Accordingly, the convergence and collection semi-angles were 9.2 mrad and 16.8 mrad, respectively. The energy resolution, defined by the full-width-half-maximum of the zero-loss peak in the EEL spectrum, was 0.15 eV. The spectra were collected by directing the beam across the whole particle with ten acquisitions of 30 ms each to prevent saturation of the charge coupled device (CCD) detector. Acquired spectra were aligned according to their ZLP and summed in post-processing.

Electron tomography datasets of particles were acquired using a Fischione 2040 tomography holder. The specimen grid was tilted through a range of - 60 degrees to + 60 degrees with 2 degree increments. ImageJ Software was used to generate the tomogram or slices through the volume, which were further segmented and surface rendered using Amira software (Visage Imaging Inc.).

TEM of cell samples. The procedure of preparing TEM sections for cellular uptake of tripods were described previously.[5] Briefly, U87MG cells were plated at 25k cells/cm^2 on the glass cover slips of the culture plate (24-well plate). When the cells were grown to 80% confluence, the U87MG cells were exposed to RGD-Au-tripod at the concentration of 5 nM in growth medium for 4 hours at 37°C. The medium was removed after incubation, and the cells were then washed twice with cold PBS and fixed in 2% glutaraldehyde and 4% paraformaldehyde in 100 mM sodium cacodylate buffer (Electron Microscopy Sciences, PA) at room temperature for 1 hour. The fixed cells on cover slips were washed and then stained with 1% osmium tetraoxide in water at room temperature for one hour. After rinsed with deionized water, the cells were stained with uranyl acetate for overnight. The cell samples were dehydrated using a graded series of ethanol in water: 50, 70, 95, and 100%, and further dehydrated in acetonitrile. The Embed 812 epoxy resin (Electron Microscopy Sciences, PA) was introduced gradually into the cell samples after dehydration. The cell samples were embed in fresh resin and polymerized in an oven at 65°C for overnight. The glass coverslips of cell samples were etched away with concentrated hydrogen fluoride (HF) for 20 min at room temperature. Semithin sections (1 µm) were cut with glass knives on a Leica Ultracut S microtome, stained with methylene blue -azure II and evaluated for areas of cells. Ultrathin sections (90 nm) were cut and retrieved on a 200-mesh bare copper grid (Ted Pella), and examined with a JEOL JEM-1400 TEM equipped with an advantage HR CCD camera operating at 80 kV.

2. Particle Size and Zeta Potential

The sizes of gold tripods and gold rods were measured using TEM and dynamic light scattering (DLS). The characterization of sizes of NPs by TEM was performed according to the standard assay protocol (NIST - NCL Joint Assay Protocol, PCC-7), including sample preparation, measurement and result analysis. A minimum of 200 discrete particles was measured from each of at least two widely separated regions of the sample. Version V1.46 of NIH ImageJ was used for image processing, analysis and measurements. The colloidal stability of nearly monodisperse dispersions of gold tripods and gold rods in hexane and aqueous solution was studied by dynamic light scattering (Malvern Zeta Size Nano S-90 DLS instrument). Absorbance values of Au and Pt were collected on a spectrophotometer using pure gold or pure platinum NPs as standards prior to making DLS measurements. The refractive indexes of gold and platinum were adapted from the Malvern Reference manual (MAN0396 Issue 1.0). The refractive index of 0.30 was adapted for gold, while the refractive index of platinum was 4.5. Since majority of Au-tripods are made of gold, we varied the refractive index from 0.3 to 4.5, the change in the size measurement was less than 5%, which was well within the experimental error. The refractive index of 0.30 was used to characterize each step of the passivation and targeting steps of NPs.

The characterization of zeta potentials ζ of NPs by DLS was performed according to the standard assay protocol (NIST - NCL Joint Assay Protocol, PCC-2).

3. Numerical analysis of the optical properties of Au-tripods and Au-rods

Numerical analysis was performed using a commercial finite difference time domain (FDTD) simulation package (Lumerical Solution Inc., Canada). A 3D non-uniform grid was used that allows for a high sampling of the field inside and in the immediate vicinity of the gold tripods or gold nanorod (grid size 0.5 nm), and for a large enough simulation volume with a side length of 240 nm (grid size > 2 nm). The simulation volume was enclosed by perfectly matched layer (PML) absorbing boundaries. A total-field/ scattered-field (TF/SF) source with a spectral pulse from 450 ~ 1450 nm and a center frequency of 432.0 THz was used to avoid diffraction artifacts from a finite source, and to have a more accurate scattered field. The light source (a total field-scattered field (TFSF)) was injected along the *y*-axis with a bandwidth of 450-1450 nm. The polarization of the source was along the z-axis. A set of power monitors in the total field region and the scattered field region were used to monitor the net power flow into the total filed region or the scattered field region, leading to the determination of the absorption cross-section or scattering cross-section, respectively. All the simulations were performed with water as the dielectric medium, with a refractive index of 1.33. A mesh-size of 0.5 nm in all the three Cartesian directions was chosen for the simulation. The centers of Pt cubic cores were placed at the origin of the coordinate system in the simulation box. Gold dielectric data was based on Johnson and Christy and platinum dielectric data was based on Palik. The ambient was water with a refractive index of 1.33. The PEG layers were ignored, because their refractive index would depend on the surface coverage, and these layers would lead to less than 10 nm peak shifts to the red. The spectral dependence of the absorption and scattering cross sections for both polarizations were calculated and added. Nanorods of a total length of 54 nm were modeled as cylinders (36 nm length and 9 nm diameter) with semi-spherical caps of constant radius of 4.5 nm. Tripod was modeled as one cubic platinum core (6.5 nm length) with three gold spheres of constant radius of 3.75 nm.

4. Cell viability test

The cytotoxicities of RGD-Au-tripods in both tumor cells (U87MG cells) and normal cells (murine fibroblast NIH 3T3 cells) were determined using a standard methyl thiazolyl tetrazolium (MTT) colorimetric assay. Basically, both cell were plated at a density of 5×10^3 cells per well in 96-well plates 24 hours prior to the exposure to the NPs. Cells were incubated in the growth media containing different concentrations of RGD-Au-tripods for 24 and 48 hours. After treatment, 3-(4,5-dimethylthiazol-2-yl)-

2,5-diphenyltetrazolium bromide (MTT, 5 mg/ml in PBS) was diluted 1:100 with medium into each well. After 4-hour incubation, culture supernatants were aspirated, and purple insoluble MTT product was redissolved in 100 µl of DMSO in 10 min. The concentration of the reduced MTT in each well was determined spectrophotometrically at 570 nm using a microplate reader (TECAN Infinite M100). Cell viabilities were presented as the percentage of the absorbance of NP-treated cells to the absorbance of non-treated cells, and plotted as concentration of RGD-Au-tripods.

5. Inductively Coupled Plasma Mass Spectrometry (ICP-MS)

The elemental analyses were performed using inductively coupled plasma mass spectrometer (ICP-MS, Thermo Scientific Xseries 2 Quadrupole). Regular NP samples were suspended in freshly prepared aqua regia (trace metal grade 70% nitric acid HNO_3:36% hydrochloric acid HCl (Fisher Scientific), 1:3/v:v) and heated until completely dissolved, and then diluted up to 8 ml with double-distilled water.

The cells pallets, homogenized tissues and organs (no more than 500 mg) were oxidized in 10 ml acid mixture (70% HNO_3 and 36% HCl at a 4:1 volume ratio) in a microwave (CEM MarsXpress Microwave Digester with Teflon microwave-safe vessels) until they were fully dissolved. The liquefied samples were then air-dried, heated and resuspended in 1 ml freshly prepared aqua regia. After a brief sonication, the mixtures were then diluted up to 8 ml with double-distilled water, and centrifuged to remove any precipitation, leaving the supernatant for gold and platinum content analyses. ICP-MS was calibrated with a series of dilutions of gold and platinum standards (Inorganic Ventures). A calibration curve against known concentrations of Au-tripods in homogenized tissues and organs was used to measure the detection limit for the gold and platinum. The detection limits for gold and platinum were below 0.5 ppb. The reproducibility of ICP-MS was confirmed by measuring a series of known concentrations of gold and platinum in homogenized tissues and organs in triplicate (Table S1).

Table S1. The accuracy of the measurement of Gold and Platinum using ICP-MS.

Known Concentration of Gold (ppb)	Measured Concentration of Gold (ppb)	Known Concentration of Platinum (ppb)	Measured Concentration of Platinum (ppb)
100	99.7 ± 0.8	100	100.2 ± 0.6
20	20.2 ± 0.4	20	19.9 ± 0.5

4	4.3± 0.3	4	4.2 ± 0.2

6. Histology and Silver Enhancement

Histological samples (heart, lung, liver, spleen, pancreas, kidney, brain, tumor) obtained after mouse euthanization were immediately fixed in 10% buffered formalin (Fisher) and then transferred to 30% sucrose in PBS. Sample processing, mounting, and hematoxyling staining were carried out using standard procedures. Briefly, histological samples were embedded in optimal cutting temperature (OCT) media and frozen in -80°C. The sections with 6~8 μm thickness were cut on the microtome (Leica CM 1850). The mounted sections were rinsed with deionized water extensively, and dried on the bench. Silver enhancement was carried out on the mounted sections prior to hematoxylin/eosin staining, using the Silver Enhancement Kit for Light and Electron Microscopy (Ted Pella). After tissue sections were rinsed with water, an equal volume of the kit's two reagents were freshly mixed first, and 50 μl was deposited on the top of the section. Enhancement was allowed to proceed for 20 min in the dark at room temperature before being stopped by rinsing with water. The treated sections were counter-stained with hematoxylin and 1% eosin (Fisher). After dehydration, the sections were mounted with Permount for viewing under an automated histology slide reading microscopy (Nanozoomer) with a 40× objective.

7. MicroPET Imaging

PET imaging was carried out on a microPET R4 rodent model scanner (manufactured by CTI Concorde Microsystems, Knoxville, TN) as previously reported.[4,6,7] PET scans were performed at 1, 2, 4, 24 and 48 hour post-injection (p.i.). U87MG tumor bearing mice were divided into six injection groups (4 mice per each group) to evaluate differences in specific targeting and biodistribution between gold tripods and gold rods, including plain tripods and rods, and RGD modified tripods and rods. For the tripod groups, each mice was injected with 3.7 MBq of ^{64}Cu-RGD-Au-tripods or ^{64}Cu-Au-tripod (200 pmol / kg of mouse body weight, or 2 mg / kg of mouse body weight, normally 5 pmol per each mouse) in 100~200 μl PBS via the tail vein. For the rod group, each mice was injected with 3.7 MBq of ^{64}Cu-RGD-Au-rods (2 mg per Kg mouse) via the tail vein. For the receptor-blocking experiment, U87MG tumor bearing mice were coinjected with 12 mg of c(RGDfC)/kg of mouse body weight and 100~200 μl of ^{64}Cu-RGD-Au-tripods or ^{64}Cu-Au tripod (200 pmol per kg mouse body weight) in PBS via the tail vein. Prior to imaging, mice were anesthetized with isoflurane (5% for induction and 2% for maintenance in house oxygen at 2L/min). Mice (4 mouse per group) were placed in the prone position and near the center of the field of view (FOV) of the scanner. The 5-min static scans were obtained at the predetermined time points after post-injection. All the PET images were then reconstructed by a two-dimensional ordered-subsets expectation maximization (OSEM) algorithm with a spatial resolution of 1.66 to 1.85 mm.[8] PET quantifications were analyzed using both AsiPro and Amide image processing software. No background correction was performed. Region of interests (ROIs, 2.5 pixels for coronal and transaxial slices) were drawn over the tumor and organs of interests on decay-corrected whole-body coronal images. Values in three to ten adjacent slices (depending on the size of different tissues or organs) were averaged to obtain a reproducible value of radioactivity concentration. The Maximum radioactivity concentration (or accumulation) within the tumor or organs of interests was obtained from the mean pixel value within combined ROIs, and were further converted to counts/ml/min using a calibration factor (calibrated for 4 mice). ROIs were then converted to counts per gram per minute based on the assumption of a tissue density of 1 g/ml, and image ROI-derived %ID/g values were determined by dividing counts/g/min by the administered activity (dose). No attenuation correction or partial volume correction were performed.

8. Biodistribution

The nude mice bearing U87MG tumor were sacrificed after 48 hour post-injection. Tumor and tissues of interest were harvested, wet-weighed and placed in scintillation vials for gamma counting (Packard/Perkin Elmer). The radioactivity uptake of the tumor or tissues of interest was calibrated against a known aliquot of radio source and expressed as a percentage of the decay corrected injection dose per gram of tissue (%ID/g). After samples underwent radioactive decay for a week, samples of tumor and tissues of interest were collected to determine concentrations of gold and platinum in each of these tissues by ICP-MS analysis (see the detailed information in ICP-MS section). The NP uptake of the tumor or tissues of interest was expressed as a percentage of injected dose per gram of tissue ((%ID/g).

9. Spectral Measurements

The extinction spectra of various NPs and methylene blue were measured using an Agilent 8453 UV-visible Spectroscopy Systems (Agilent Technologies) with a wavelength range of 190 to 1100 nm and a resolution of 1 nm. The extinction cross section (σ_e, sum of absorption and scattering) was calculated from the extinction spectrum.

10. Photoacoustic Imaging (PAI)

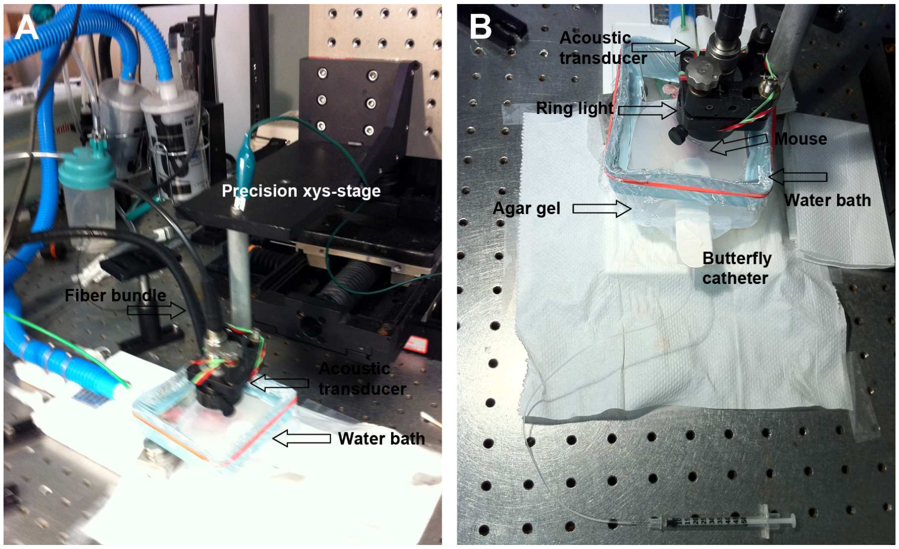

Figure S2. Photoacoustic Imaging Instrument. (A) in vivo photoacoustic imaging setup, (B) the mouse was lying on its left side (left lateral recumbent) and partially embedded in Agar gel covered with a water bath.

Photoacoustic Imaging System. The custom-built photoacoustic instrument was described previously and is shown in Figure S2.[9-11] A tunable pulsed laser with a repetition rate of 10 Hz and a pulse width of 5 ns (Nd:YAG Surelight-III-10 connected to Surelite OPO Plus, Continuum) was focused on the phantom samples or the tumor of mouse through a fiber optic ring light guide (50-1353 Ringlight, Fiberoptic Systems, one inch focal length, one cm focal spot diameter). The average laser light intensity in the range of 670~900 nm wavelengths was measured to be ~4 mJ/cm^2 on the sample surface. A 5

MHz focused transducer (A309S, 25.5 mm focal length, 4 MHz bandwidth, 2.0 F number, 6.5 mm depth of focus, Panametrics-Olympus NDT) was placed, without intercepting the light path, inside the fiber optic ring light guide to acquire photoacoustic imaging in reflection mode. The transducer provides 600 μm lateral resolution and 380 μm axial resolution. A precision xyz-stage (U500, Aerotech Inc.) was used to move the transducer and the fiber ring along a planar 2D trajectory with minimum step size of 0.5 mm. The photoacoustic signal (A-scan, signal as a function of depth along z-axis) was acquired and averaged over 16 laser pulses. The time of arrival and the intensity of the laser pulses as function of time were recorded using a silicon photodiode (DET10A, Thorlabs). This information was used to synchronize the acquisition and compensate for pulse-to-pulse variations in laser intensity. The analogue photoacoustic signals (A-Scans) were amplified using a 40 dB preamplifier (Panametrics, 5676/115VAC) and digitized using a digitizer/oscilloscope (Infinium 54825A, Agilent). For reconstruction of the photoacoustic and ultrasound images, the A-scan from each position of the transducer was bandpass-filtered with 100% fractional bandwidth, compensated for laser intensity variation and envelope detected, and was then combined to reconstruct a 3D intensity image of the target. No further post-processing was carried out on the images. The ultrasound images acquired using the 5 MHz and 25 MHz transducers were aligned together using small vertical translations so that the object's skin level matched in both images. The photoacoustic and high-frequency ultrasound images were analyzed, co-registered, and displayed using AMIDE[12] software.

11. Photoacoustic signal linearity characterization of Au-tripods and Au-rods

Polyethylene capillaries (I.D. = 0.76 mm, O.D. = 1.22 mm, one-inch long, Becton Dickinson Co. MD) were filled with various NPs or methylene blue through a syringe with a 22G needle. Both ends of the filled tubing were quickly sealed by a hot plate, and then embedded in the 1% agarose gel (Figure S3). We constructed three agarose phantoms: one with inclusions of aqueous solution of Au-tripods at increasing concentrations from 0.1 nM to 25.6 nM, one with inclusions of aqueous solution of Au-rods at the same concentrations (normalized by sample weight), the last one with inclusions of aqueous solution of methylene blue at increasing concentrations from 2.5 μM to 80 μM. After the tubing arrays were made on the solidified gel, another layer of ~3 mm of 1% liquid agarose was poured on the top of the phantom to seal and protect the tubing arrays. The phantom was then positioned inside a water tank. A tunable pulsed laser with a repetition rate of 10 Hz and a pulse width of 5 ns was focused on to the phantom samples. The average laser light intensity at the range of 670 to 1000 nm wavelengths was measured to be ~4 mJ/cm2 on the sample surface. The photoacoustic images (10 mm × 120 mm) of phantoms were acquired at 670, 700, 725, 750, 800, 850, and 900 nm with step size of 0.25 mm. For methylene blue, the phantom PA images were obtained at 670 and 700 nm. The photoacoustic and high-frequency ultrasound images were analyzed, co-registered, and displayed using AMIDE[12] software. Three-dimensional cylindrical ROIs at the size of the inclusion were used to calculate the photoacoustic signal from each sample.

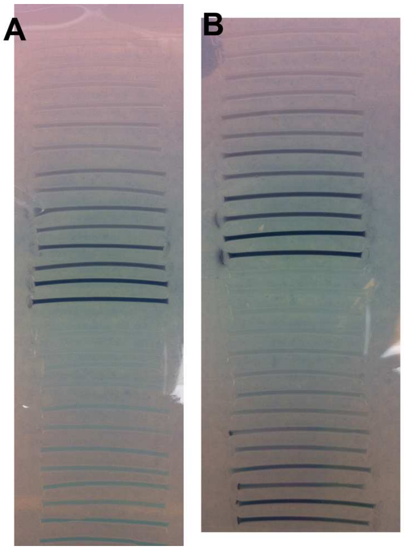

Figure S3. Phantoms of Au-tripods and Au-rods for photoacoustic signal linearity characterization. (A) Phantom of Au-tripods and methylene blue, (B) phantom of Au-tripods and Au-rods.

12. *In vitro* targeting of RGD-Au-tripods (PAI and ICP).

U87MG cells were placed at 10 × 10^3 cells/cm2 on the Petri dishes (60 mm, Becton Dickinson Co. MD) and grown to ~80-90% confluence. RGD-Au-tripods at different concentrations of 0.25, 1 and 4 nM in 5 ml of growth media was added to the culture dishes in triplicate and incubated with U87MG cells at 37□C in the 5% CO_2 incubator for 0.5, 1, 2 or 4 hrs. The control studies included U87MG cells exposed to either plain Au-tripods or saline. For the blocking experiment, U87MG cells were pretreated with 20 µM c(RGDfC) for 10 min prior to adding RGD-Au-tripods. After washed with PBS three times, cells were detached by trypsine (TripLE express, Invitrogen) and harvested by centrifuge. Cells were counted with a hemocytometer. The cell pellets were resuspended in 50 µl of PBS and mixed well with 50 µl of 1% liquid agarose at 42°C, and quickly transferred to 100 µl indentations in the pre-prepared agarose gel, which were prepared by the tube mold to form 100 µl wells in the gel. After cell suspension was completely solidified, the phantom was sealed with a final 3 mm of agarose gel to seal the wells and protect the content of each well. The phantom was then positioned inside a water tank. Typical photoacoustic imaging conditions were same as the previous ones. The photoacoustic images (50 mm × 100 mm) of phantoms were acquired at 675, 700, and 725 nm with step size of 0.25 mm. The cellular uptake of tripods was quantified by measuring photoacoustic intensity of each sample. Finally, the indentations with cell suspensions were cut from the gel and then lysed by nitric acid and aqua regia. The cellular uptake of tripods was further quantified by measuring Au and Pt content in each sample using ICP-MS.

13. Limit of Detection for Tripod-targeted U87MG cells

U87MG cells were placed at 10×10^3 cells/cm^2 on the Petri dishes (100 mm, Becton Dickinson Co. MD) and grown to ~80% confluence. The cells were exposed to 4 nM RGD-Au-tripod in growth medium for 4 hours at 37°C in the 5% CO^2 incubator. After incubation, the cells were washed three times with cold PBS to remove unbound NPs, and cells were detached by trypsine (TripLE express, Invitrogen) and harvested by centrifuge. Cells were counted with a hemocytometer. The cell were resuspended in PBS and diluted to a serial of cell concentrations (from 11.5×10^3 to 368×10^3 cells) with PBS ($n = 3$ samples per concentration). Each 50 µl of cell suspension was mixed well with 50 µl of 1% liquid agarose at 42°C, and quickly transferred to 100 µl indentations in the pre-prepared agarose gel. After cell suspension was completely solidified, the phantom was sealed with a final 3 mm of agarose gel and positioned inside a water tank. Typical photoacoustic imaging conditions were same as the previous ones. The photoacoustic images (50 mm × 100 mm) of phantoms were acquired at 670, 700, 725, 750, 800, 850, and 900 nm with step size of 0.25 mm. Quantitative analysis of the photoacoustic signal from the phantom revealed the limit of detection of tripod-loaded U87MG cells. Finally, the indentations with cell suspensions were cut from the gel and then lysed by nitric acid and aqua regia. The detection limit was further confirmed by measuring Au and Pt content in each sample using ICP-MS.

14. Photoacoustic detection of Au-tripods in living mice.

The RGD-Au-tripods at six different concentrations were mixed with matrigel (Matrigel Basement Membrane Matrix, Phenol Red-free, Becton Dickinson) at 1:1 ratio preparing tripod solution at 0.39, 0.78, 1.56, 3.125, 6.25, and 12.5 nM. The resultant mixtures were quickly injected subcutaneously (30 µl) to the right hind side of mouse (*n* = 3). After the incisions were solidified in their place, the mouse was placed on its left side (left lateral recumbent) and partially embedded in the agarose gel covered with a water bath (Figure S3), and was then scanned under the photoacoustic system. A photoacoustic image with lateral step size of 0.25 mm was acquired using the 5 MHz transducer at 670, 700, and 725 nm wavelength. Following the photoacoustic scan, an ultrasound image was acquired using the 25 MHz transducer. The photoacoustic and ultrasound images were analyzed, co-registered, and displayed using AMIDE software. Three-dimensional ROIs over the inclusion volume based on the ultrasound images were used to calculate the photoacoustic signals. The volume of the ROIs was kept at 30 mm^3, which is equivalent to the 30 µl of injection volume.

15. RGD-Au-tripod tumor targeting in living mice.

Two groups of female nude mice (*n* = 3 in each group, 6-8 weeks old) were inoculated subcutaneously at their right hind side with 5×10^6 U87MG cells in 50 µl of PBS. The tumors were allowed to grow to a volume of 150 ~200 mm^3. The mouse was placed on its left side (left lateral recumbent) and partially embedded in the agarose gel covered with a water bath (Figure S3), and was then scanned under the photoacoustic system. Before the injection, the photoacoustic and ultrasound images of the mice were taken. A photoacoustic image with lateral step size of 0.25 mm was acquired using the 5MHz transducer at 670, 700, and 725 nm wavelength. Following the photoacoustic scan, an ultrasound image was acquired using the 25 MHz transducer. The U87MG tumor bearing mouse was then injected with 100~200 µl of RGD-Au-tripods (200 pmol per kg mouse body weight) in PBS through the tail-vein using a butterfly-catheter to avoid any position change during the injection (50 µl of dead volume) (Figure S3B). For the receptor-blocking experiment, mice were co-injected with 12 mg of c(RGDfC) / kg of mouse body weight and 100~200 µl of RGD-Au-tripods (200 pmol per kg mouse body weight) in PBS through the tail-vein. After injection, photoacoustic images (20 mm × 20 mm) of phantoms were acquired at 670, 700, and 725 nm with step size of 0.25 mm were acquired at 0.5, 1, 2, and 4 hours post-injection. Following the photoacoustic scan, the ultrasound images were acquired to confirm the scan area. The photoacoustic and ultrasound images were analyzed, co-registered, and displayed using AMIDE software. Quantitative analysis of the photoacoustic signal from the tumor was done by drawing three-dimensional ROIs of interest around tumor based on the ultrasound images. After 4 hour post-injection, the mice were sacrificed, and tumor and tissues of interest were collected for histology study (see more information in Histology and Silver Enhancement section), elemental analysis (see more information in ICP-MS section) and TEM (see more information in Microscopy section).

16. Pathologic Evaluation

The female BALB/c mice were obtained from Charles River Laboratories for pathologic evaluation. Mice with four animals per cage were housed in carefully monitored and maintained environmental conditions throughout the study (66 ± 2°F temperature; 39 ± 1% relative humidity; 12-hour light/dark cycle). The mice were randomly allocated into two experimental groups. In the first group, mice were given a 200 μl intravenous injection (via the tail vein) of sterile saline; in the second group, mice were given a 200 μl intravenous injection of 20 pmol Au-tripods (~200 μg of total weight based on the ICP result).[13] Mice were carefully monitored throughout the study. For each mouse, their body weight, physical appearance, behavior and interactions toward other animals were assessed and recorded twice per week. At each time point after injection (1 day, 1 week, and 6 weeks), four mice per group were euthanized via carbon dioxide asphyxiation. Blood was collected immediately after confirmed death via cardiac puncture for hematology analysis and serum biochemistry analysis. Necropsies were performed for gross pathologic evaluation and collection of major organs and tissues (heart, lungs, brain, kidneys, liver, spleen, pancreas). All of major organs and tissues were fixed in neutral-buffered 10% formalin for 48 hours, and were then routinely processed and stained with Hematoxyline and Eosin H&E (Histotec Laboratories) for light microscopy. Histopathological examination was performed by a veterinary paathologist. Histopathologic diagnosis was performed according to the Standardized System of Nomenclature and Diagnostic Criteria (SSNDC).

C. Supplementary Data and Discussion

1. Characterization of Nanoparticles

1.1. Particle size of cubic Pt NPs

Because the size and shape of Pt NPs are critical to this seed-mediated process, it is very important to first obtain monodisperse Pt NPs with desired shapes. Sun and coworkers reported a facile route to prepare monodisperse Pt NPs with tunable size from 3 nm to 7 nm. The shape and size of resultant Pt NPs are strongly dependent on reaction temperature at which a trace amount of iron pentacarbonyl ($Fe(CO)_5$) was injected. The trace $Fe(CO)_5$ was believed to facilitate fast nucleation and improve homogeneous growth of platinum, ending up with monodisperse Pt NPs. However, we found that it was hard to control their sizes and shapes during the synthesis of large Pt NPs (bigger than 6 nm). At the low reaction temperature, the unexpected low-nucleation during the synthesis of large NPs often results in poor, inconsistent, and non-reproducible quality of Pt NPs. In order to improve the quality, we used small Pt NPs with high quality as seeds to grow the large Pt NPs (Scheme S2). Typically, the 4.9 nm Pt NPs (Pt NP-A) were injected into the reaction mixture containing Pt precursor, followed by injection of trace $Fe(CO)_5$. Finally, truncated cubic Pt NPs became large cubic ones (6.5 nm, Pt NP-C) with same quality (Figure S4). The large Pt NPs (Pt NP-D) with size more than 7.5 nm can also be obtained when 6 nm Pt NPs were used as seeds. All of the cubic Pt NPs have a very narrow size and shape distribution (Figure S4, S5, and Table S2). The lattice fringes of all four Pt NPs shown in Figure S4 are c.a. 0.195 nm and related to (200) planes of Pt in fcc phase.

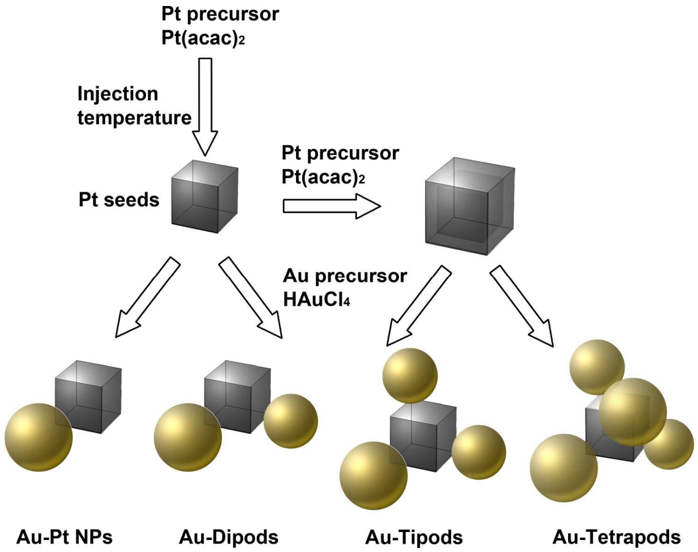

Scheme S2. Illustration of synthesis of Pt seeds and branched Au nanostrutures.

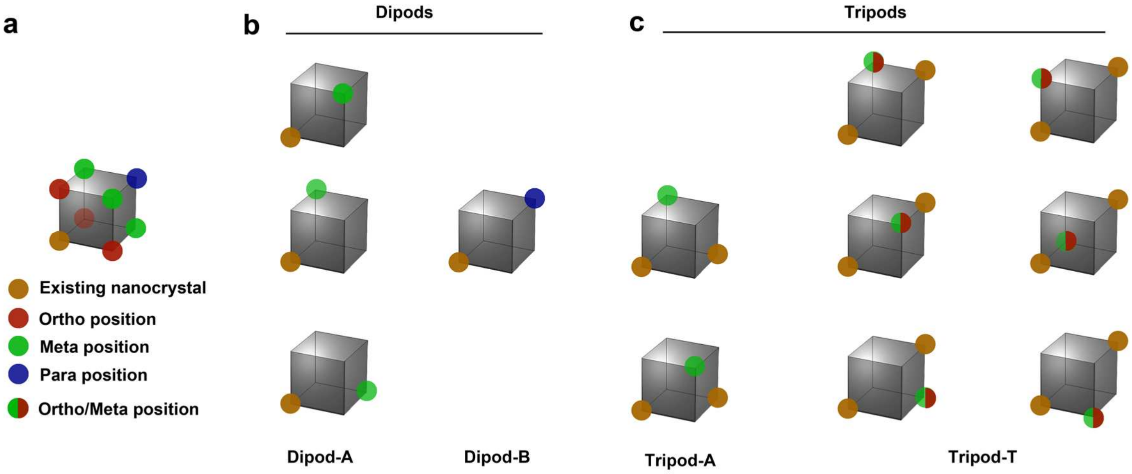

Scheme S3. Illustration of potential nucleation positions of cubic Pt NPs (a) and possible geometrical configuration of resultant dipods (b) and tripods (c). Gold color dot represents the existing nanocrystal. Red color dots represent the ortho positions relative to the existing gold dot. Green color dots represent the meta positions relative to the existing gold dot. Blue color dot represents the para positions relative to the existing gold dot. Green/red mix dots represent the meta/ortho positions relative to two existing gold dots.

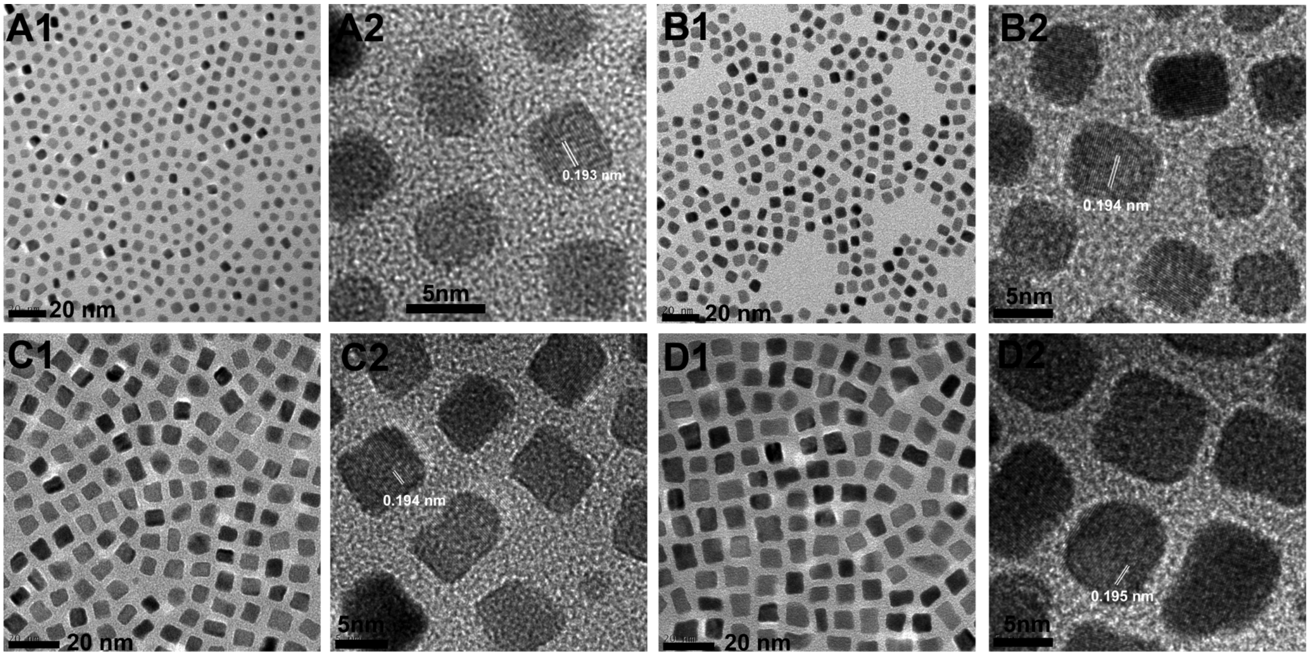

Figure S4. Image analysis of Pt NPs. Representative TEM images of 4.9 nm truncated cubic (A1), 5.8 nm truncated cubic (B1), 6.5 nm cubic (C1) and 7.5 nm cubic (D1) Pt NPs. The Representative HRTEM images of corresponding Pt NPs were shown in A2-D2. The lattice fringes in the HRTEM images were corresponding to the (200) lattice planes.

Table S2. Mean diameters and standard deviation of various Pt NPs. The particle diameters were determined by TEM analysis and DLS (See the method section in Supporting Information B.2).

Pt NPs	Size by TEM* (nm)	Size by DLS (nm)
Pt NP-A	4.89 ± 0.28	5.6 ± 0.77
Pt NP-B	5.84 ± 0.21	6.0 ± 0.63
Pt NP-C	6.50 ± 0.36	6.8 ± 0.89
Pt NP-D	7.62 ± 0.51	7.7 ± 1.11

* A minimum of 200 discrete particles was measured from each of at least two widely separated regions of the sample.

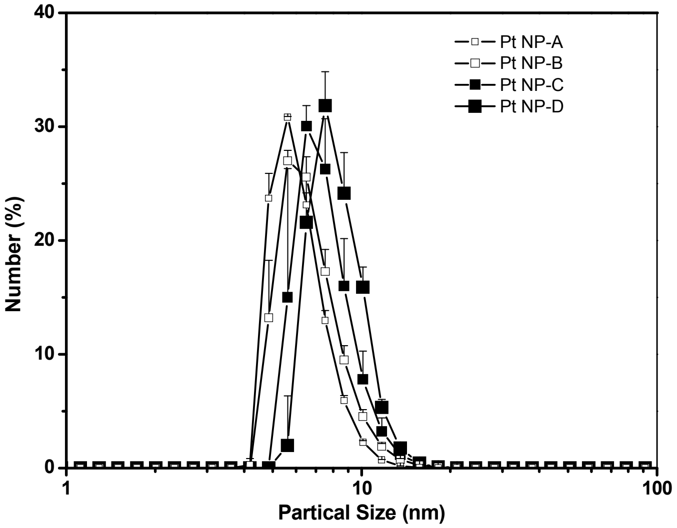

Figure S5. Particle size and distribution of various Pt NPs (See the Figure S4).

1.2. Synthesis and Characterization of Branched Au-nanostructures

The use of Pt NPs with stringently controlled sizes and shapes as seeds results in various Au hetero-structures with controlled shapes, such as dumbbell-like Au-Pt NPs, Au-dipods, Au-tripods, or Au-tetrapods (Figure 1a and 1b). As Sun and coworkers described previously, the larger Pt NPs ended up with more complex nanostructures. Typically, the epitaxial growth of Au on 4.9 nm Pt seeds produced dumbbell-like Au-Pt NPs. Use of 6 nm Pt NPs as seeds resulted in Au-dipods. Au-tetrapods could be obtained when 7.5 nm Pt NPs were used as seeds. Although there are several possible nucleation positions at the vertices of cubic Pt seeds (Supporting Information Scheme S3), the incoming constitutional Au crystal tends to nucleate at the para or meta positions instead of ortho positions relative to the existing Au crystal, due to potential steric hindrance. There are two geometrical isomers; one is linear and the other is bent (Figure 1), corresponding to para and meta configurations, respectively. Even though there are more meta than para positions, the steric effect partially cancels out the difference in the nucleation possibilities, resulting in roughly equal amounts of two isomers of Au dipods (n, total number of counted particles = 300, $p > 0.2$). There were two types of symmetries observed in Au-dipods (which can be represented by simple geometries modeled as cubic cores with three spheres as shown in Figure 1a): one with C_{2v} (dipod-A) and the other with D_h (dipod-B, regardless of the geometry of cubic core). Interestingly, we found that, unlike 7.5 nm Pt NPs resulting in a mixture of tripods and tetrapods, 6.5 nm Pt seeds almost exclusively led to formation of tripods with a narrow distribution of size and shape (Figure S6-C, Figure S7). The statistic analysis suggested that majority (more that 70%) of resultant nanoparticles were tripods (Figure S8).

TEM and HR-TEM were used to determine the size and size distribution of various branched gold NPs using an image processing program (ImageJ). A minimum of 200 discrete particles was measured from each of at least two widely separated regions of TEM images of various branched gold NPs. Since the various branched gold NPs have non-spherical shapes, their digitized micrographs needed to be first transformed from grey-scale image into a binary image consisting of discrete non-spherical particles and background. By selecting appropriate threshold values, the NP size was determined by measuring the number of contiguous pixels that met the criteria for a particular NP shape. The area (the number of pixels) was then converted into the equivalent circular diameter assuming an uniformly spherical particle. The equivalent circular diameter and the circularity value (defined as $4\pi A/P^2$, where A is the particle area and P is its perimeter, a value of 1.0 indicates a perfect circle; as the value approaches 0.0, it indicates an increasingly elongated polygon), of various branched gold NPs were shown in the Table S3.

Table S3. Summary of Size measurement of various branched Au NPs by TEM and DLS.

NPs	Equivalent circular diameter (nm)	Circularity*	Size by DLS (nm)	Size of individual component measured by HR-TEM	
				Length of cubic Pt (nm)	Diameter of spherical Au (nm)
Au-Pt NPs	9.18 ± 0.19	0.68 ± 0.11	8.0 ± 0.8	4.84 ± 0.36	6.47 ± 0.31
Au-dipods	10.37 ± 0.52	0.60 ± 0.08	9.3 ± 0.9	5.91 ± 0.24	6.89 ± 0.23
Au-tripods	12.51 ± 0.63	0.51 ± 0.07	10.2 ± 1.0	6.44 ± 0.41	7.84 ± 0.37
Au-tetrapods	14.22 ± 0.75	0.57 ± 0.12	12.2 ± 1.8	7.70 ± 0.46	8.78 ± 0.55

*circularity value is defined as $4\pi A/P^2$, where A is the particle area and P is its perimeter, a value of 1.0 indicates a perfect circle; as the value approaches 0.0, it indicates an increasingly elongated polygon.

We then performed the dynamic light scattering (DLS) and statistical analysis based on TEM images for measuring the sizes of various Au multipods. The sizes and shapes of various Au-multipods and each component within NPs were determined by DLS and TEM (Supporting Information Table S3). In order to determine the particle shape, the outline of particle shape of two-dimensional (2D) projection TEM images was analyzed by image analysis software (ImageJ, Supporting Information Figure S7). The resultant measurements such as shape factors (circularity) allow us to distinguish branched NPs from the spherical NPs. Circularity varied from a value of 0.7 for simple dumbbell Au-Pt NPs (like spherical nanoparticles) to 0.5 for highly branched multipods. The Au-tripods showed the lowest circularity among the branched NPs (Supporting Information Table S3), largely due to their anisotropic nanostructures and surface roughness. Although it is difficult to measure the thickness of branched NPs to determine their volume, the equivalent circular diameters were used to quantify the size change of branched multipods. It is also noticed that the size of Au-tripods obtained by DLS is smaller than the 2D projection size by TEM analysis (Supporting Information Table S3 and Figure S9), but is close to the corresponding equivalent circular diameter. This is mainly attributed to the fact that the measured diameter of a nonspherical particle from DLS is the diameter of a sphere that has the same translational diffusion speed as the particle.

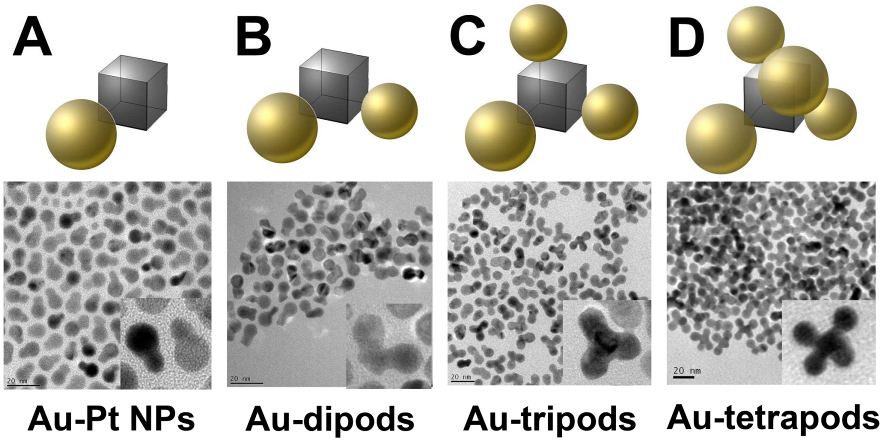

Figure S6. TEM of dumbbell Au-Pt, Au-dipods, Au-tripods, and Au-tetrapods.

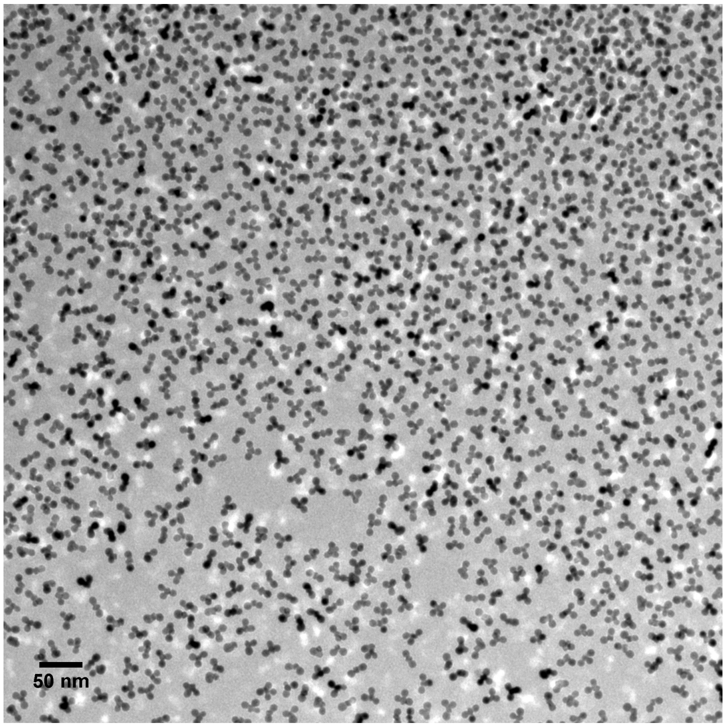

Figure S7. Representative TEM of Au-tripods. The monodisperse Au-tripods showed uniform shapes and narrow size distribution.

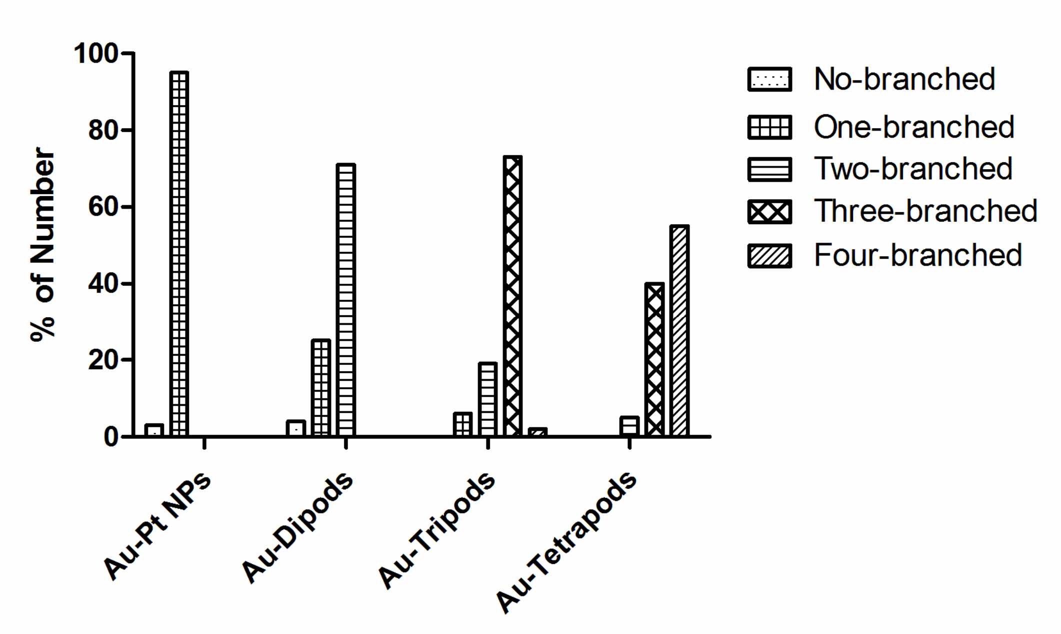

Figure S8. Statistic number of particles with different Au-branch numbers. The results were obtained by counting a minimum of 200 discrete particles on TEM images.

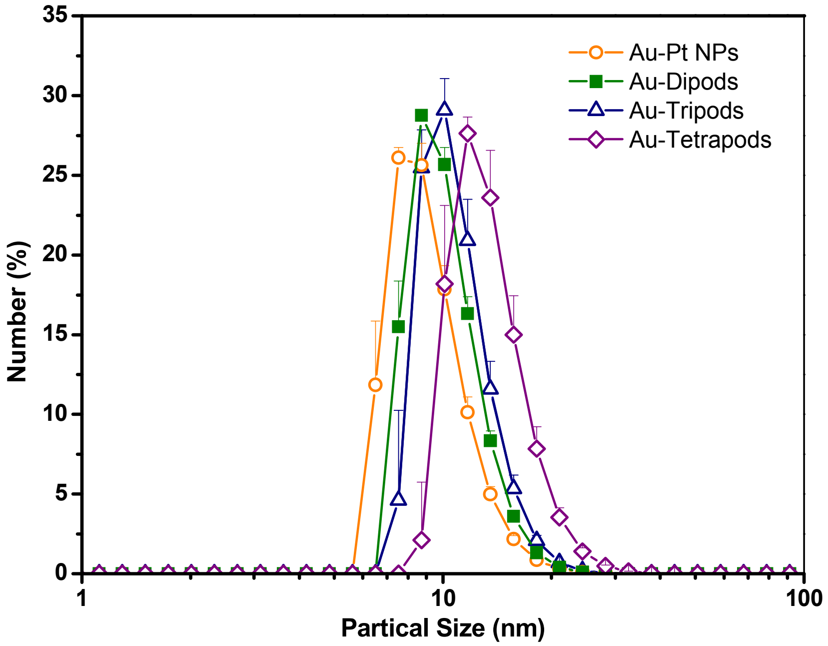

Figure S9. Partial size and distribution of dumbbell Au-Pt, Au-dipods, Au-tripods, and Au-tetrapods.

Unlike the other heterogeneous nucleation and growth, where different shapes could be achieved by tuning the seed-to-precursor ratio and controlling the heating profile, the growth of Au-multipods on Pt NPs is directed by the lattice direction of Pt seeds. The growth along the preferential lattice directions (i.e. (111)) is faster than that along other directions, leading to branched structures (multi-pods). The representative HR-TEM and scanning STEM images of Au-Tripods showed that well crystallized interfaces had been formed between the Pt seeds and grown Au branches because of their very similar lattice constants in an fcc phase (Figure S10). The lattice fringes between Pt seeds and Au branches shown in Figure S11 are c.a. 0.23 nm and related to (111) planes of either Pt or Au in the fcc phase. STEM images clearly showed that each Au branch epitaxially grew on one of the corners of cubic Pt seeds.

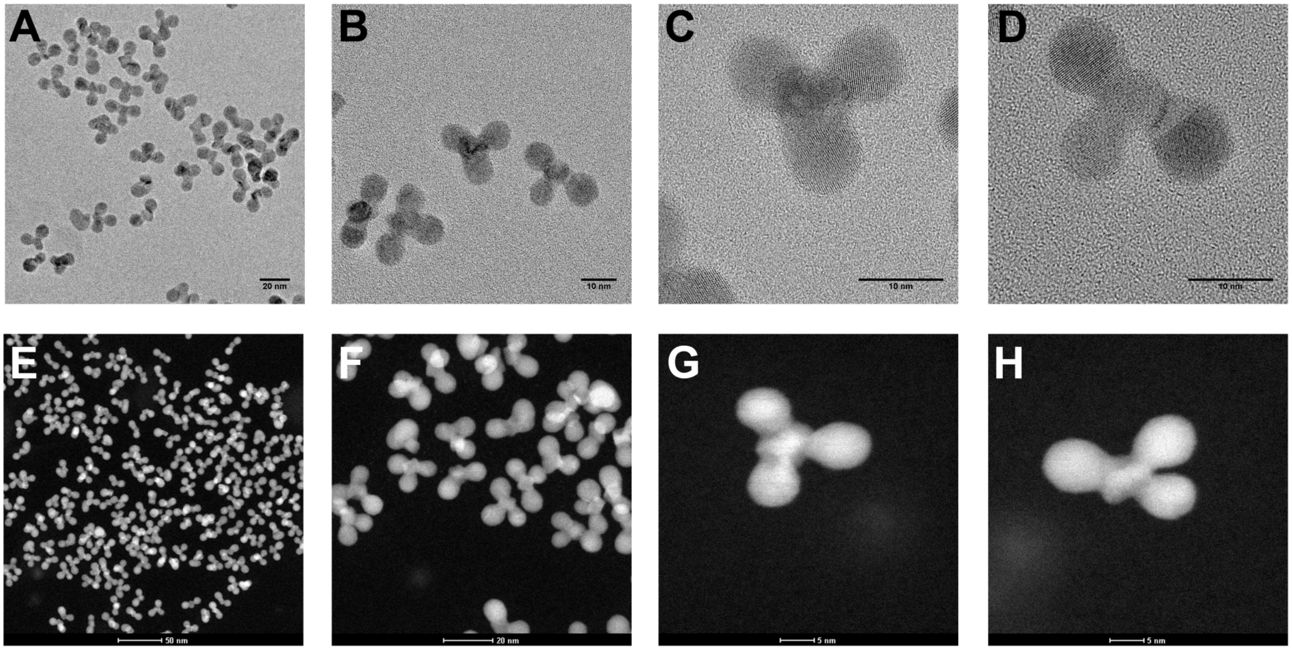

Figure S10. The representative HR-TEM (A-C) and scanning STEM images (E-H) of Au-Tripods showed that well crystallized interfaces had been formed between the Pt seeds and grown Au branches

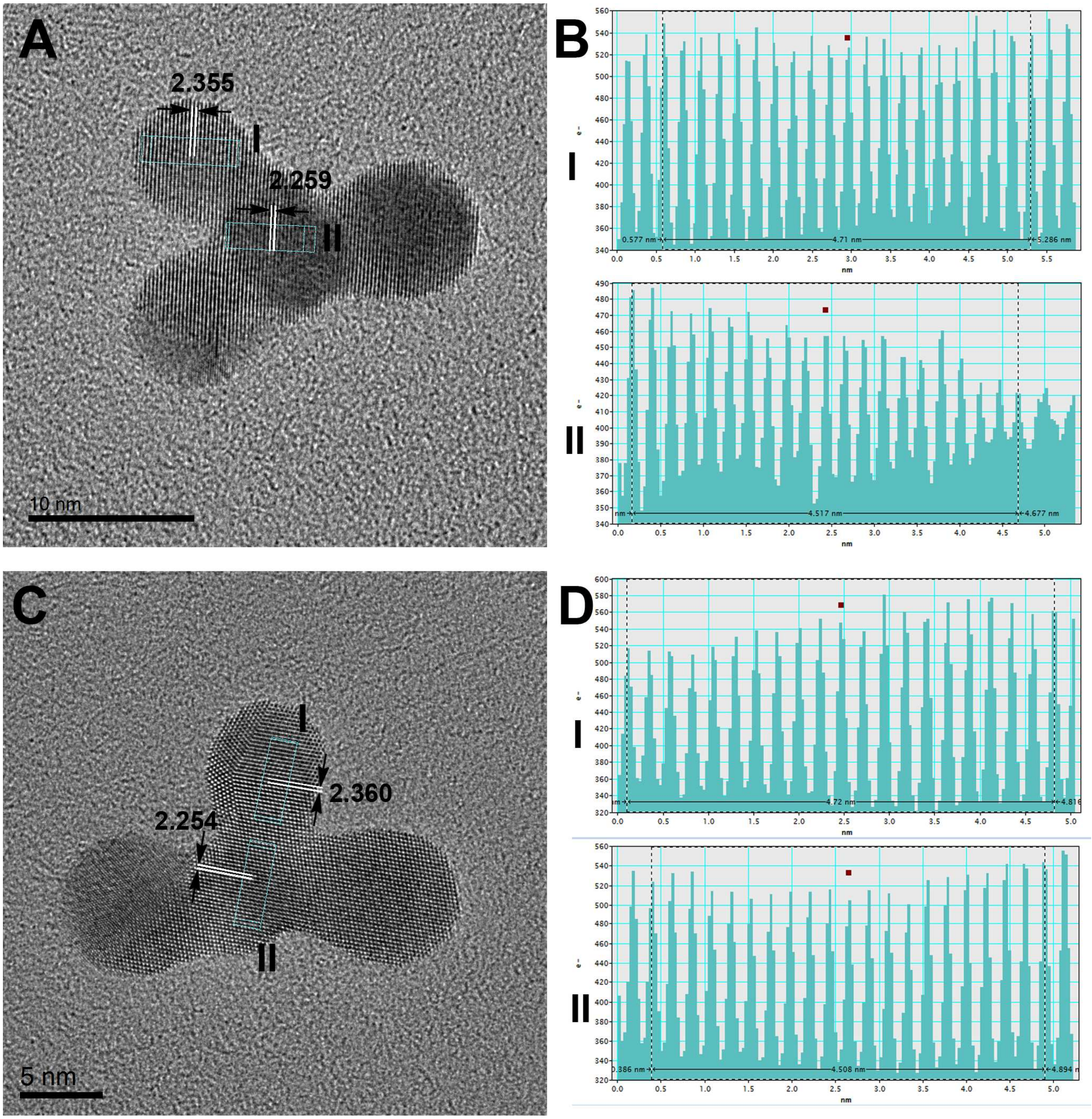

Figure S11. HRTEM of Au-tripods.

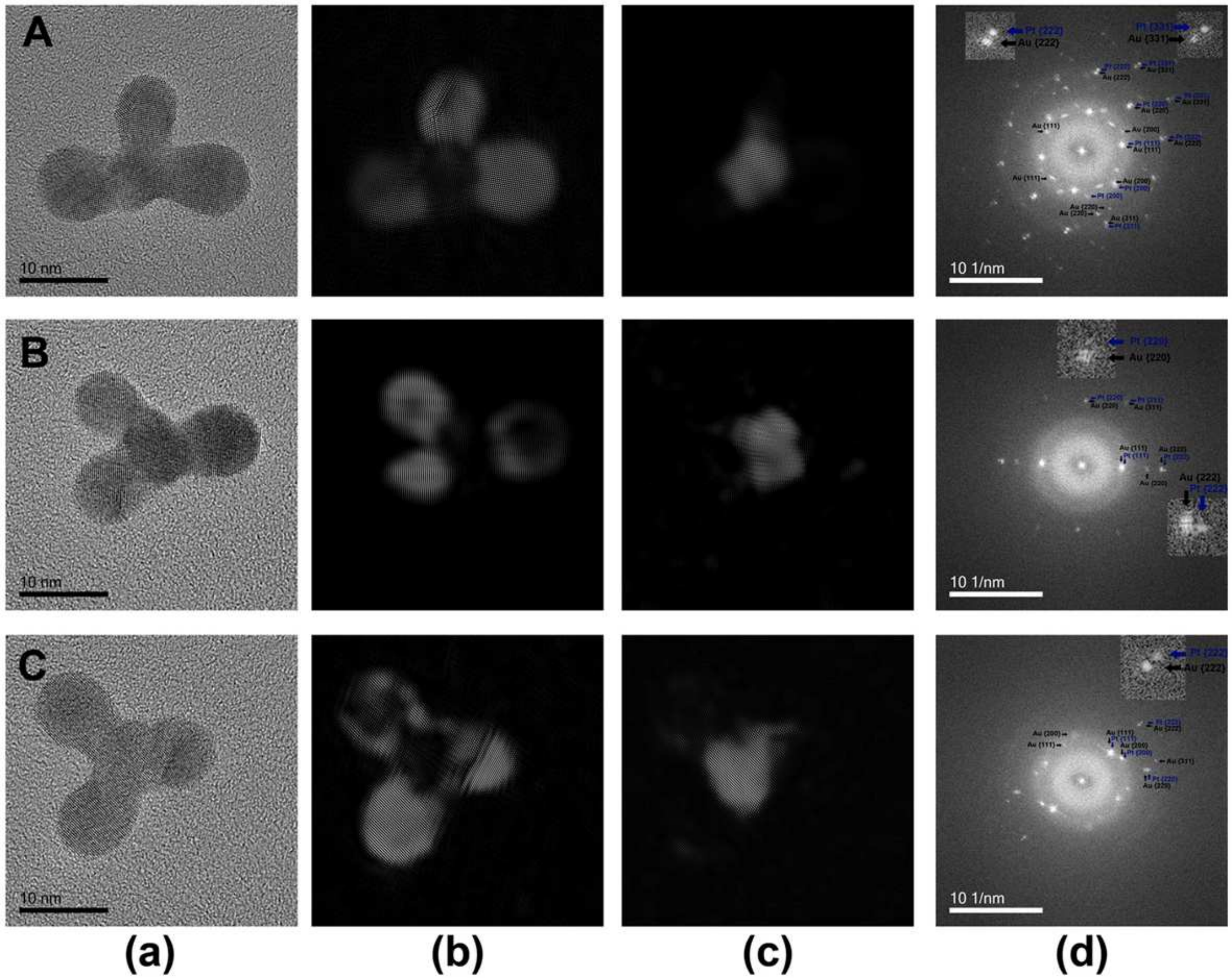

Figure S12. HRTEM and FFT images of typical Au-tripods.

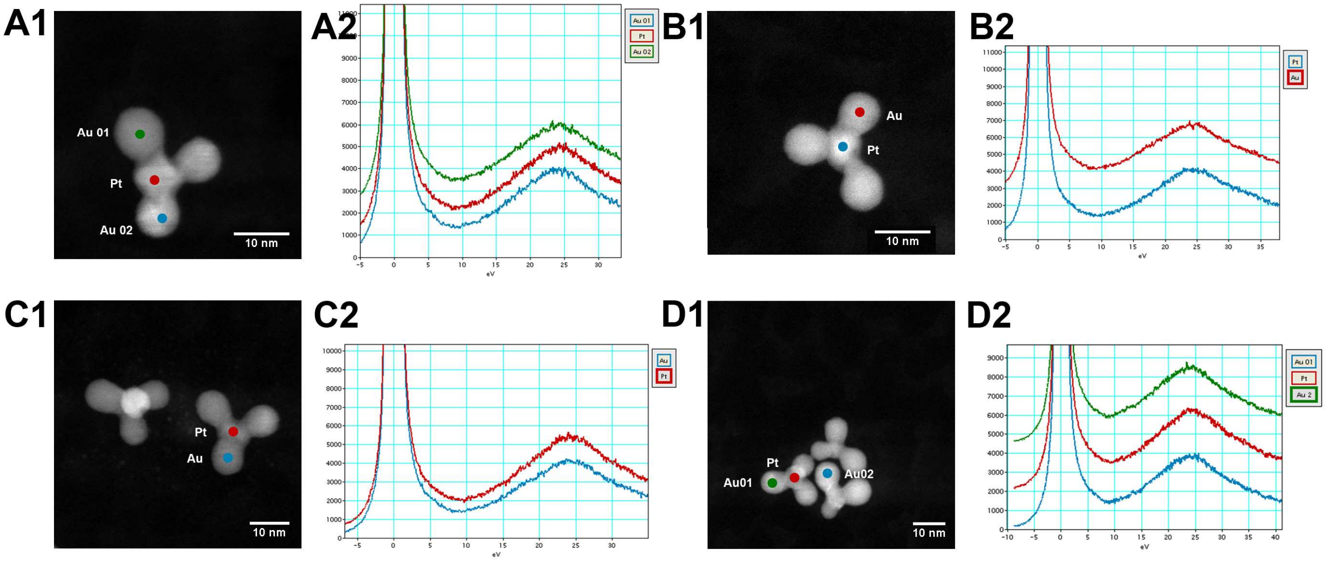

Figure S13. STEM and EELS of typical Au-tripods. The Au branches and Pt seeds could be distinguished by STEM-EELS (Figure S13). It further confirmed that the epitaxial growth of Au on Pt seeds preferentially happened on Pt (111) planes.

In order to determine the dependence of plasmon resonances on local structure and composition, we performed STEM-electron energy loss spectroscopy (EELS) spectra of the tripods in the low-loss region (Figure S13). Three different beam positions for acquiring low-loss EELS spectra are marked as 'Au01', 'Pt', and 'Au02'. Figure S13b showed the spectra corresponding to the three beam positions after deconvolution with a vacuum pre-measured -zero loss peak (an EELS zero-loss peak (ZLP) full-width at half-maximum of 0.15 eV). Beam position 'Au01' and 'Au02' provided surface plasmon resonance (SPR) peaks at c.a. 2.35 eV, which corresponds to a wavelength of around 527 nm (typical for SPR for gold nanoparticles using UV-Vis spectrometer), while SPR peak of beam position 'Pt' was very close to gold ones but slightly weaker and broaden toward lower energies. UV-Vis studies showed that there was no clear SPR observed for monometallic Pt NPs. It was believed that the presence of Pt in tripods might cause spread and attenuation of the SPRs. A shoulder peak of beam position 'Au01' and 'Au02' at 1.75 eV was observed and attributed to a wavelength of around 700 nm.

2. Characterization of Gold Nanorods

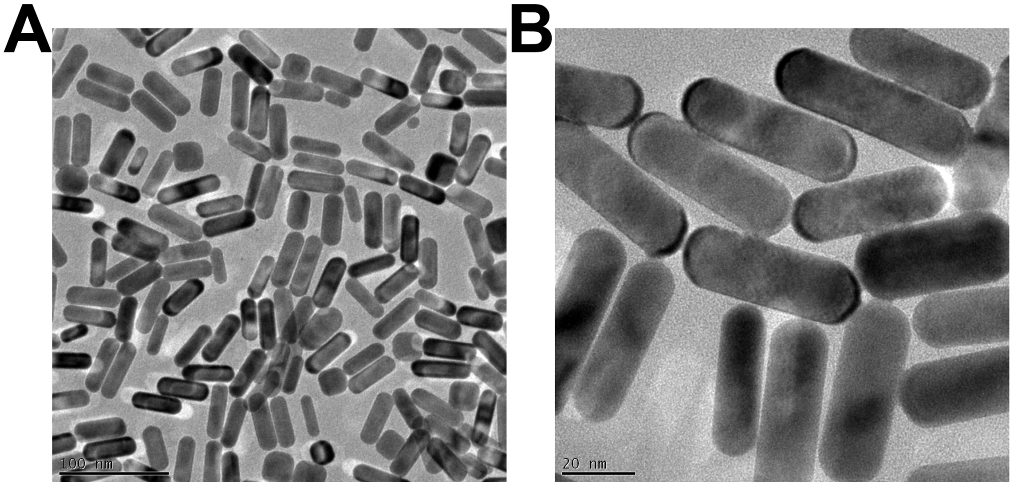

Figure S14. TEM of typical Au-rods in the low resolution (A) and in the high resolution (B).

3. Determination of concentrations of tripods and rods

Nanorods of a total length of 54 nm were modeled as cylinders (36 nm length and 18 nm diameter) with semi-spherical caps of constant radius of 4.5 nm. Tripods were modeled as cubic cores (6.5 nm length) with three spheres of constant radius of 3.75 nm. The molar atom weight of nanorods and tripods were calculated based on the ideal models identified by TEM (See more information in the previous section). The ratio of gold to platinum weight of tripods was determined by ICP-MS. The weight of single NP was determined by its ideal geometry shape and the density of individual component. The molar atom weight of nanorods is 1.42×10^8 g/mol; the molar atom weight of tripods is 1.11×10^7 g/mol. The actual weight concentrations of tripods and rods were determined by ICP-MS (See the ICP-MS section). Based their molar atom weight of tripods and rods, their molar concentrations were calculated accordingly.

4. Optical properties and simulation

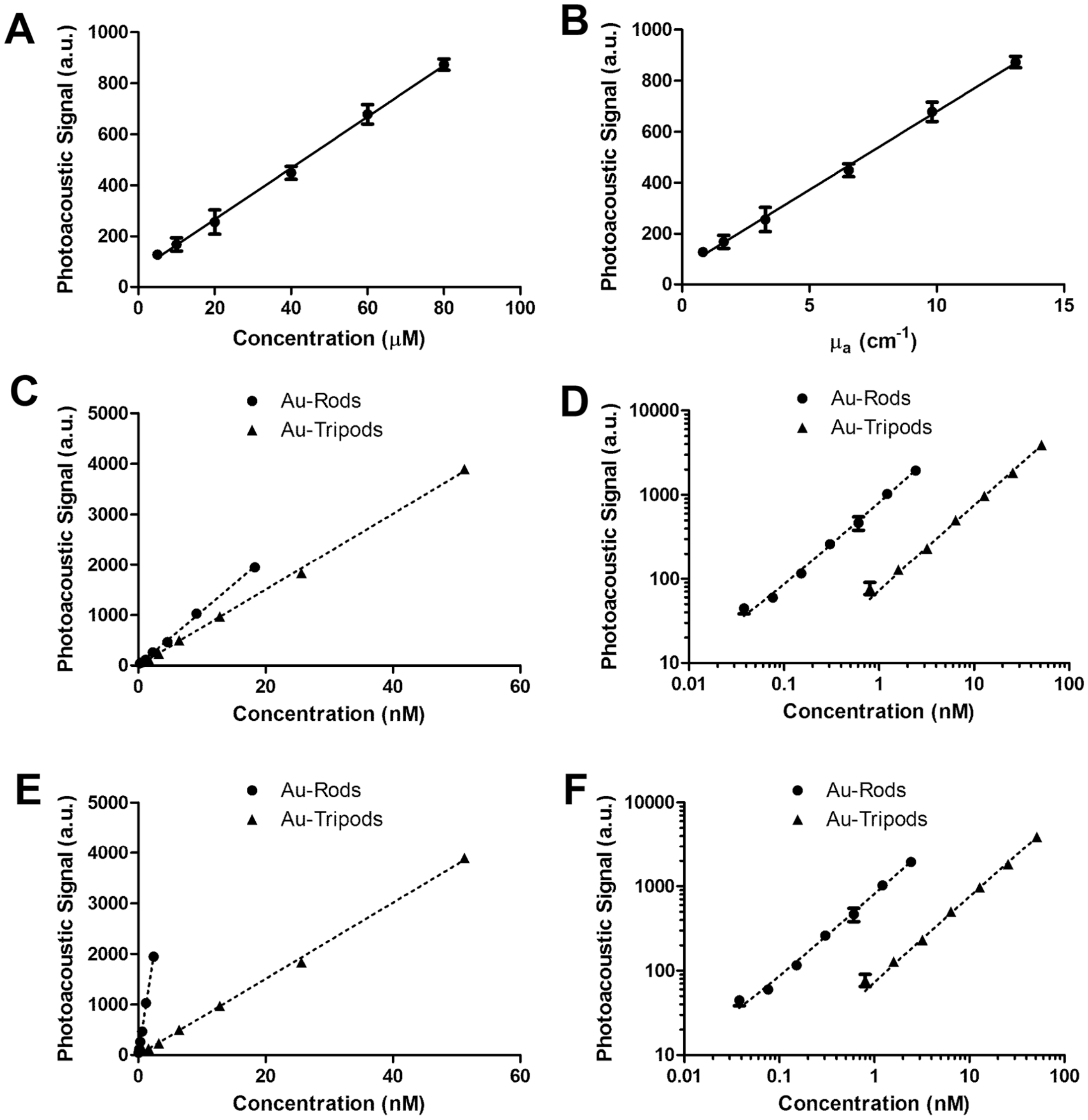

Figure S15. Measuring the optical absorption cross sections of Au-tripods by photoacoustic imaging. **a**, A plot of the PA amplitude against the concentration of methylene blue. **b**, The linear relationship between the optical absorption coefficient (μ_a) and PA signal amplitude derived from the plot of (**a**) and the known σ_a of methylene blue. **c**, Plots of PA signal amplitude versus weight concentration for Au-tripods and Au-rods. **d**, The linear relationship between PA signal amplitude and weight concentration derived from the plot of (**c**). **e**, Plots of PA signal amplitude versus molar concentration for Au-tripods and Au-rods. **f**, The linear relationship between PA signal amplitude and weight concentration derived from the plot of (**e**).

$$\mu_a = 0.01626 \times PA\ signal - 1.0556$$

$R^2 = 9.984E\text{-}01$

$$PA\ signal\ of\ Au\ rods = 803.8 \pm 12.3 \times Conc.\ of\ Au\ rods + 5.758 \pm 13.04$$

$$PA\ signal\ of\ Au\ tripods = 75.26 \pm 1.08 \times Conc.\ of\ Au\ tripods - 2.859 \pm 24.13$$

Table S4. Comparison of the optical cross sections of Au-rods and Au-tripods at a wavelength of 670 nm

	Cross section (10^{-15} m^2)		σ_a/σ_e
	Extinction (σ_e)	Absorption (σ_a)	
Au-rods	2.24±0.04	2.01±0.03	0.90
Au-tripods	0.206±0.003	0.202±0.003	0.98

The results were measured at 670 nm.

Number ratio of Au-tripods to Au-rods normalized by sample weight = 13.2:1

Ratio of absorption cross section of Au-tripods to Au-rods normalized by sample weight = 1.33

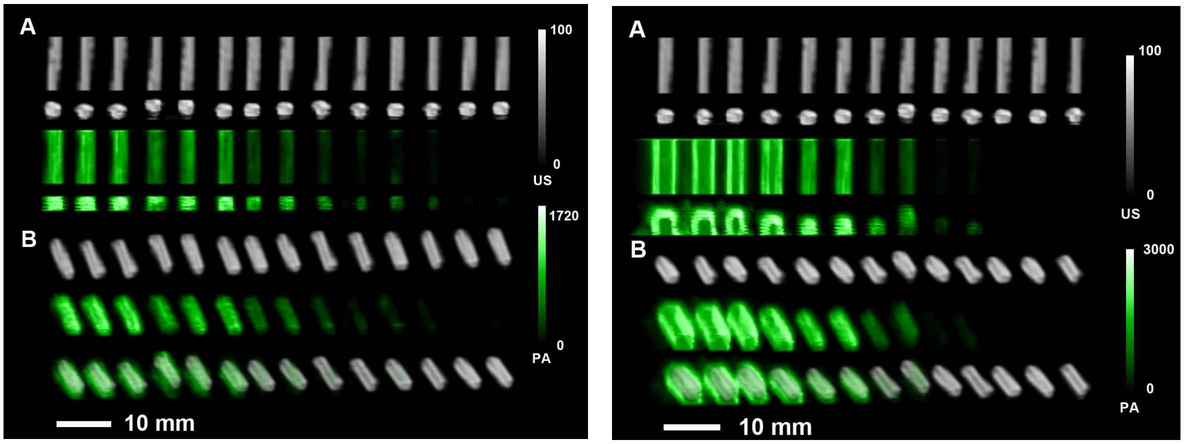

Figure S16. Photoacoustic (PA) phantom images of Au-tripods (right panel) and Au-nanorods (left panel) based on the same sample weight. Three-dimensional reconstructions of typical PA phantom images were shown from different angles of views (A: front view; B: tilt view).

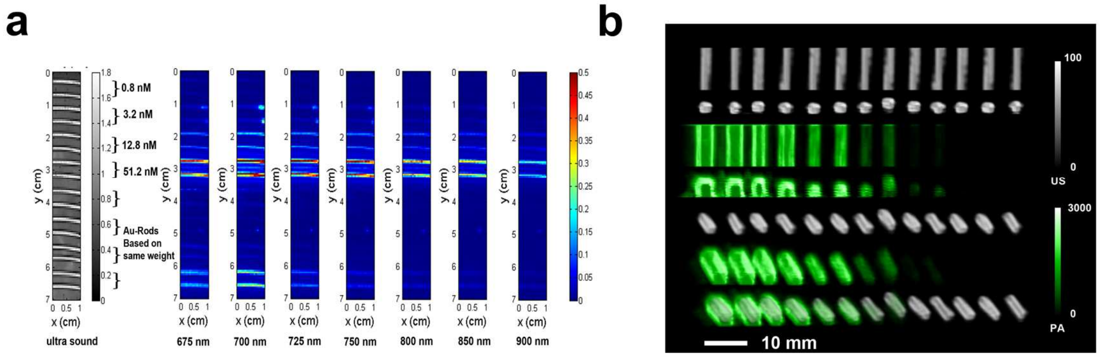

Figure S17. (a) Photoacoustic (PA) phantom images of Au-tripods and Au-nanorods based on the same sample weight. (b) Three-dimensional reconstructions of typical PA phantom images of Au-tripods.

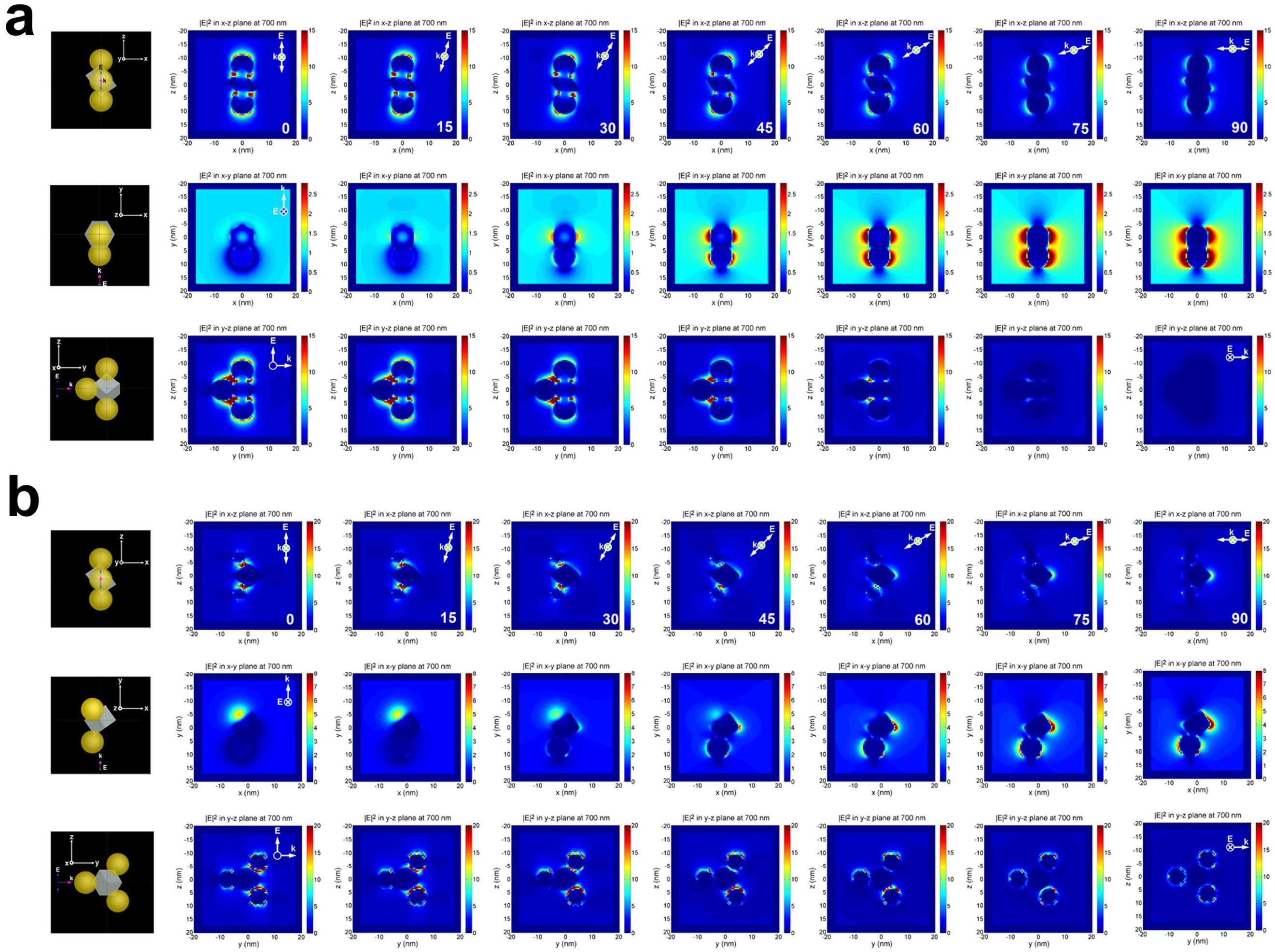

Figure S18. **a** and **b**, Polarization dependence of the average electric field intensity of tripod-T and tripod-A. Electric field intensity contours in xz plane, xy plane and yz plane at 700 nm were obtained from the FDTD calculations on both tripod-T and tripod-A. The long axis of tripod-T is parallel to the z-axis; one of side of tripod-A is parallel to the z-axis. From left to right, the excitation polarization relative to the z-axis is 0, 15, 30, 45, 60, 75, and 90°, respectively. x and y represent the horizontal and vertical lengths of the calculated area.

Discussion of optical properties and simulation

Since the contributions of scattering cross-sections to extinction cross-sections is much smaller than those of absorption cross-section, the absorption cross-sections were used to evaluate the optical properties of tripods. As anisotropic nanostructures, the rotation of Au-tripod-T in the range of 0° to 90° caused reduction for the cross-sections at 700 nm because of significant difference between their longitudinal mode and transverse mode (Supporting Information Figure S18). Due to the symmetric structure of tripod-A, however, their cross-sections did not change much as a function of the rotational angle.

In order to further clarify the effect of the geometric shapes of the tripods on their optical cross-sections, two types of tripods, initially perpendicular to the incident beam or their long axis parallel to the e-field, rotated around the x-axis at certain angles (the angle between z-axis and their long axis is 0°, 15°, 30°, 45°, 60°, 75°, or 90). The electric field intensity contours were calculated at the excitation wavelength of 700 nm as the excitation polarization was varied gradually from the longitudinal to transverse directions. It was clear that under the resonance excitation, the maximum field enhancement regions were observed to rotate away from vertical tripod as the excitation polarization rotated around y-axis. The cross-section for the longitudinal modes of tripod-T is almost an order of magnitude higher compared to those of the transverse modes (Figure 3c). This is because the strength of the dipolar resonances created under longitudinal excitation is much higher than those created under transverse excitation. The polarization dependence of the cross-section was also observed for tripod-A, although the effect was little less than that of tripod-T.

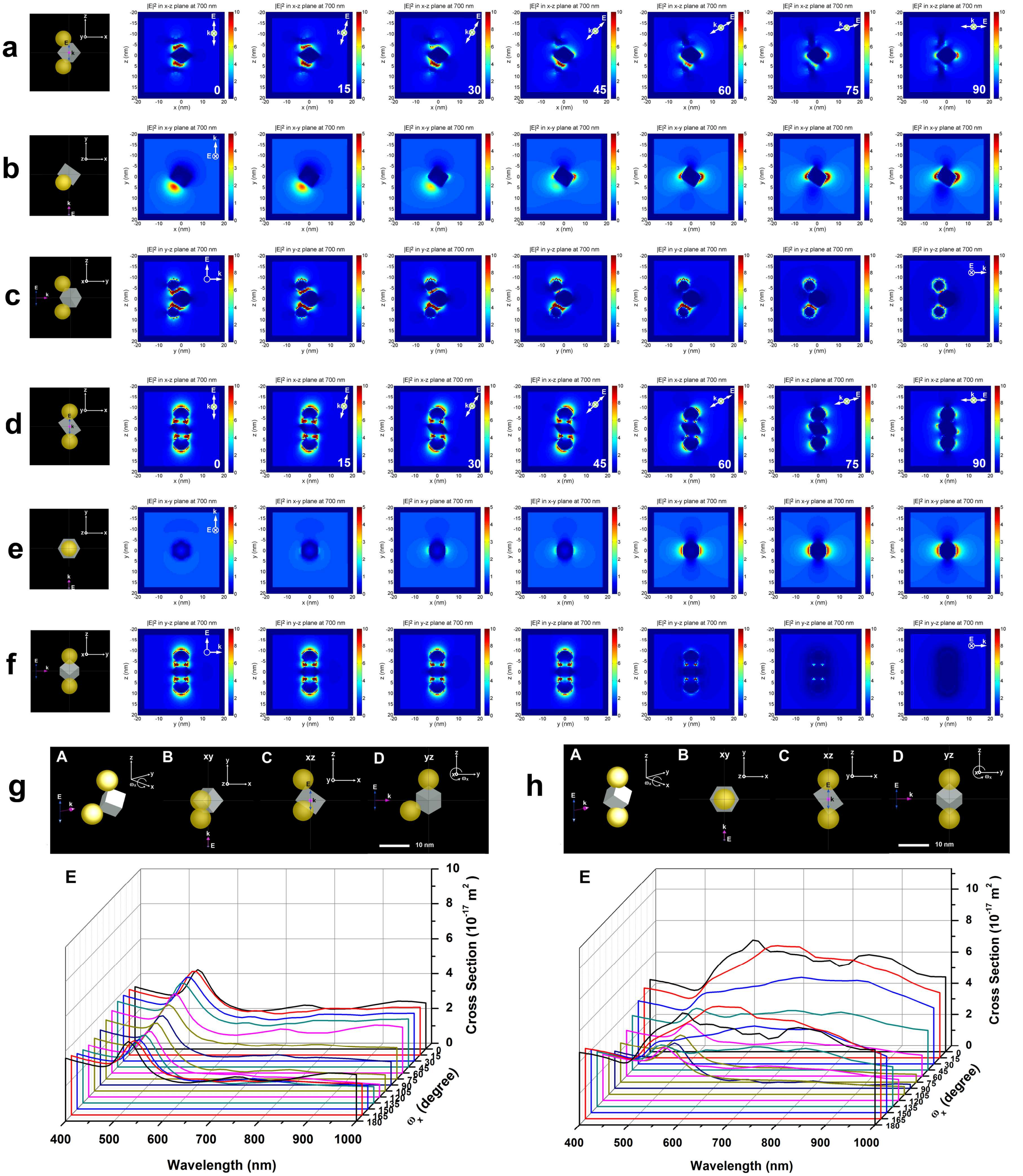

Figure S19. Polarization dependence of the average electric field intensity of dipod-A (a-c) and dipod-B (e-g). Electric field intensity contours in xz plane, xy plane and yz plane at 700 nm were obtained from the FDTD calculations on both dipod-A and dipod-B. From left to right, the excitation polarization relative to the z-axis is 0, 15, 30, 45, 60, 75, and 90°, respectively. x and y represent the horizontal and vertical lengths of the calculated area. (g) The calculated absorption cross-section of dipod-A as a function of ω_x (the incident beam is polarized along the z-axis, and the dipod-A is rotated around the x-axis. ω_x is the angle between the e-field and the long axis of dipod-A. (h) The calculated absorption cross-section of dipod-B as a function of ω_x (the incident beam is polarized along the z-axis, and the dipod-B is rotated around the x-axis. ω_x is the angle between the e-field and the long axis of dipod-B.

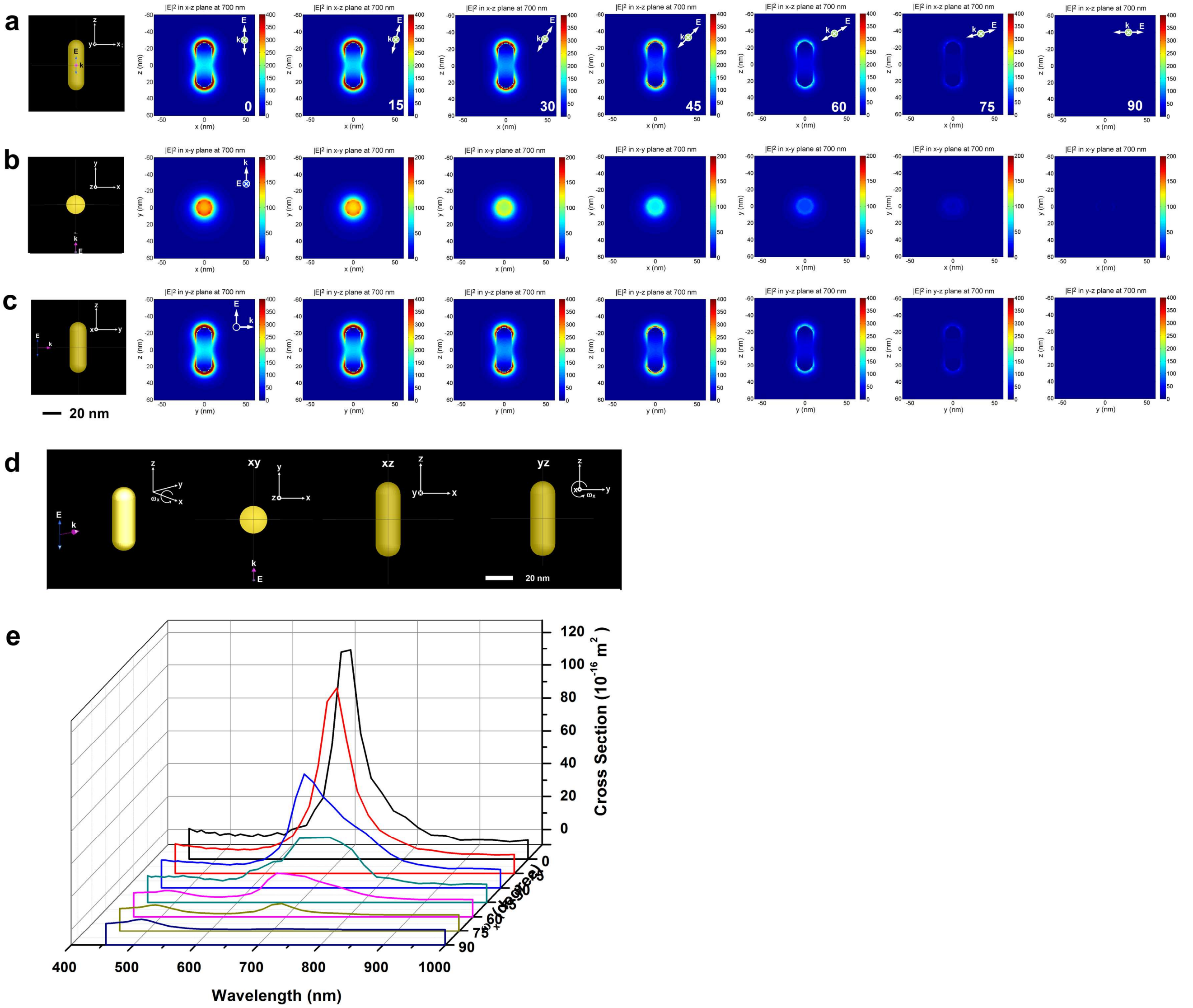

Figure S20. Polarization dependence of the average electric field intensity of Au-rods (**a-c**). Electric field intensity contours in xz plane, xy plane and yz plane at 700 nm were obtained from the FDTD calculations on Au-rods. From left to right, the excitation polarization relative to the z-axis is 0, 15, 30, 45, 60, 75, and 90°, respectively. The x and y represent the horizontal and vertical lengths of the calculated area. (d-e) The calculated absorption cross-section of Au-rods as a function of ω_x (the incident beam is polarized along the z-axis, and the Au-rods is rotated around the x-axis. ω_x is the angle between the e-field and the long axis of Au-rods.

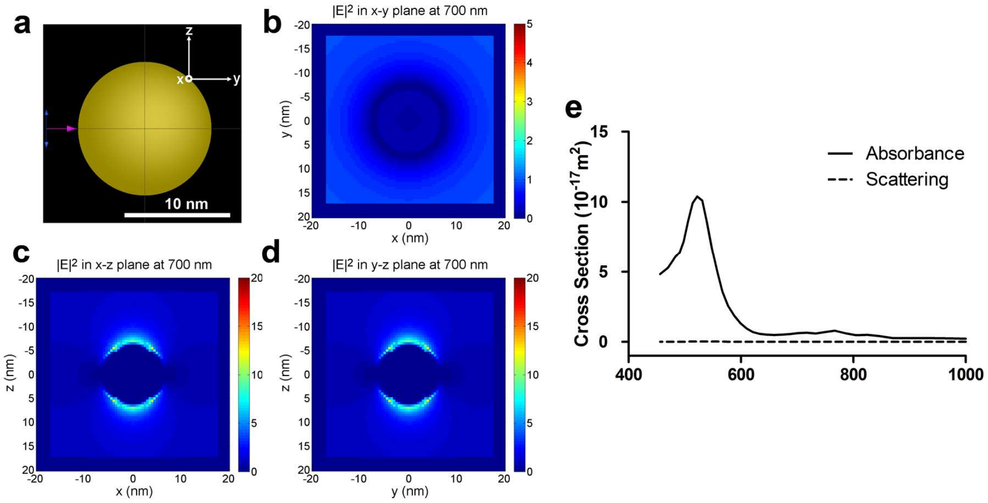

Figure S21. a, Schematic gold nanospheres based on the same volume of Au-tripods are modeled by Lumerical FDTA Solution (Lumerical Solution Inc.). **b-d,** Electric field intensity contours in xz plane, xy plane and yz plane at 700 nm were obtained from the FDTD calculations on gold nanospheres. The incident beam is polarized along the z-axis. The x and y represent the horizontal and vertical lengths of the calculated area. **e,** The calculated absorption cross-section of gold spheres as a function of wavelength.

5. PEGylation of Au-tripods

5.1. PEG coating

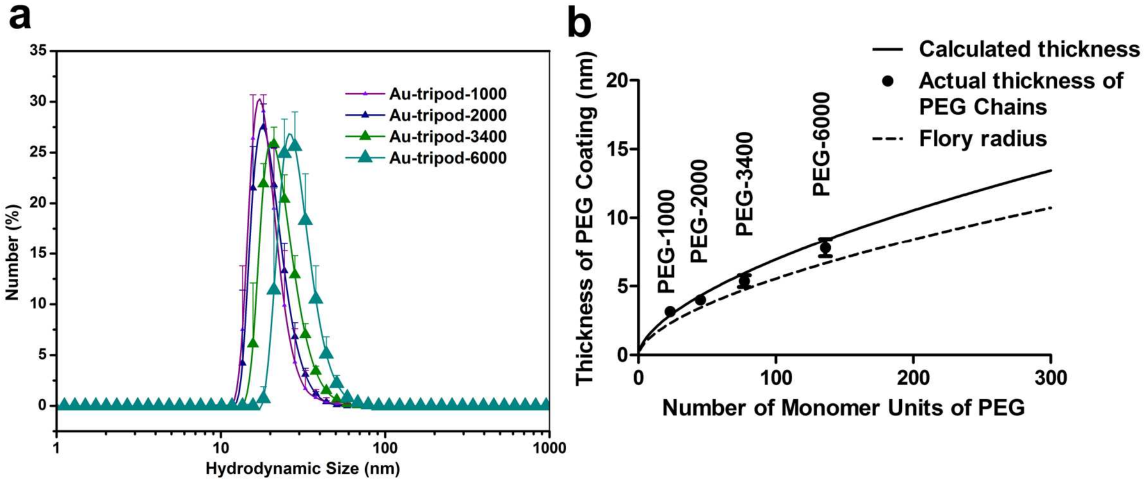

Figure S22. Hydrodynamic size and PEG coating thickness of PEGylated Au-tripods. **a**, Hydrodynamic size of Au-tripod coated with different PEG chains (PEG = 1000, 2000, 3400, and 6000). **b**, The thicknesses of various PEG coatings on the Au-tripods. The solid curve shows the increase of calculated thickness of coated PEG layer as a function of the number of monomers (N). Flory radius (R_f) of the PEG coil: $R_F = \alpha \cdot N^{0.6}$, where α is the length of a monomer unit (3.5Å). The thickness (L) is calculated from Flory radius: $L = (\pi/2)^{1/2} \cdot R_F$.[14] The dash curve shows the increase of Flory radius of the PEG chain as a function of the number of monomers.

Table S5. Particle sizes and zeta potentials of various PEGylated Au-tripods.

Au-tripod-x (x = MW)	Avg. number of monomers of PEG chain	Hydrodynamic size (nm)	Zeta Potential (mV)
Au-tripod-1000	23	16.70 ± 0.19	26.50 ± 0.7
Au-tripod-2000	45	18.21 ± 0.52	25.38 ± 0.5

Au-tripod-3400	77	20.84 ± 0.63	24.56 ± 0.4
Au-tripod-6000	136	25.82 ± 0.75	21.70 ± 0.9

In order to stabilize the gold-based NPs in the aqueous solution and provide the capability for subsequent surface modification, we developed a facile, versatile PEGylation strategy which can significantly increase *in vivo* circulation time of resultant NPs and reduce their reticuloendothelial system accumulation versus uncoated counterparts. The PEGylation of gold-based NPs involved the preparation of bidentate thiol-terminated polyethylene glycol (PEG) chains and their surface assembly/coating process, which was believed to be attributed to a robust covalent interaction between gold and sulfur-containing PEG linkers.[15] Here, we optimized the condition for the PEGylation of gold-tripods and studied how PEG length affected the stability of resultant NPs in the aqueous solution. Initially, four different heterofuncitonal bidentate thiol-terminated PEG chains (with the weight average molar mass: 1000, 2000, 3400 and 6000 Da) were synthesized according to the literature procedure with slight modification.[16] Utilizing excess amount of PEG diamine for the incorporation of bidentate thiol group at one of amine groups significantly minimized the formation of the bisubstituted species. Various monosubstituted PEGs (*O*-(3-aminopropyl) polyethylene glycol lipoate amide, LPA-PEG-x-NH2, x = 1000, 2000, 3400, or 6000) were easily obtained through the chromatographic purification and extensively characterization by MALDI spectroscopy (Figure S1 and S2).

The PEGylation of gold-based nanoparticles involves the formation of gold-thiolate bonds at the gold-sulfur interface and the self-assembly of a monolayer on gold surface. Understanding this process at the nano-scale is critical for functionalization and biocompatibility of gold surface for specific bioconjugation. Here, the behavior of PEG grafted on gold surface was confirmed by DLS (Method section). As expected, the hydrodynamic sizes of PEGylated Au-tripods increased as the grafted PEG chain length was increased (Figure S20 and Table S5). The thickness of the grafted PEG layer on the tripod surface was determined according to the size differences between PEGylated Au-tripods and unmodified ones. As seen in Figure S19b, the thickness increased as a function of the number of monomers and correlated with the Flory radius (F) ($R_F = \alpha \cdot N^{0.6}$, where α is the length of a monomer unit (3.5Å) and N is the number of monomers), which is used to describe the conformation of PEG layer. The calculated thickness of grafted PEG layers is derived from Flory radius : $L = (\pi/2)^{1/2} \cdot R_F$.[14] Based on the grafting density, the PEG chains on the surface show two main conformations: 'mushroom' conformation and 'brush' conformation. The latter one has a higher graft density that the former one.

The transition from mushroom conformation to brush conformation occurs when the distances between the PEG chains are less than Flory radius.

5.2. Quantification of PEG density on PEGylated Au-tripods.

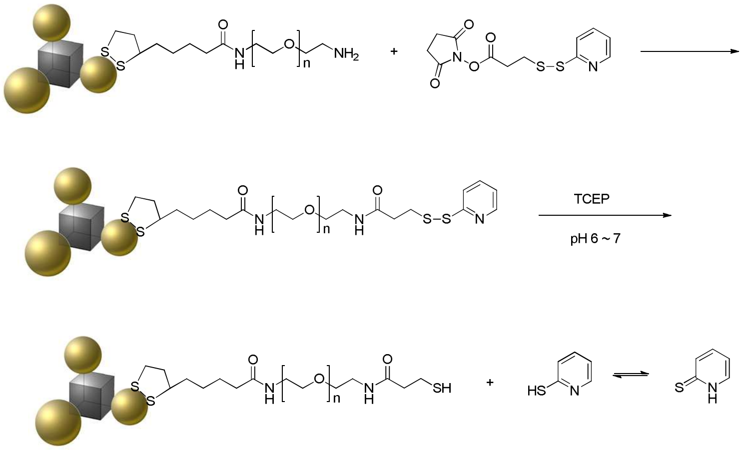

Figure S23. Quantification of amino groups on tripods.

Coupling-cleavage method. The water-soluble Au-tripods (Au-tripod-PEG-3400-NH2, 50 nM, 0.5 ml, 2.5 × 10^{-11} mol, see the determination of concentrations of tripods) in 10 mM PBS (pH = 7.2) were treated with 10 mM *N*-succinimidyl 3-(2-pyridyldithio) propionate (SPDP) in 0.5 ml of acetonitrile solution under a nitrogen atmosphere and stirred for 4h at room temperature. The activated Au-tripods were purified by a centrifugal-filter (Amicon centrifugal filter device, MWCO = 10 kDa) and washed 3 times by repeating the centrifuge/dispersion step, in order to completely remove excess SPDP and byproduct. The purified Au-tripods were resuspended in 0.5 ml of PBS and treated with 10 mM TCEP for 2 hours at room temperature. The thiol-reactive portion (2-pyridyldithio group) of SPDP reagents reacted optimally with free sulfhydryls or TCEP, resulting in displacement of a pyridine-2 thione group (TP), the concentration of which was determined by measuring the absorbance at 365 nm (the molar extinction coefficient of the TP was 7000 $M^{-1}cm^{-1}$ at 365 nm in the experimental condition). The filtrate was collected by a centrifugal-filter (Amicon centrifugal filter device, MWCO = 10 kDa), and the absorption of the released TP was measured at 365 nm by a UV-vis spectrometer. The tripods without coupling SPDP were treated in the same condition and used as control samples in the spectrophotometric analysis. The spectral measurement was done in triplicate. Assuming that all of the amine groups on the PEGylated tripods were accessible to the SPDP crosslinker, and the yields of the coupling reaction with SPDP and cleavage reaction with TCEP were 100%, the number of amine groups should be equal to the number of cleaved TP groups after tripods were treated with TCEP. Despite the optimal condition, this method of determining amine groups underestimated the actual number of amine groups (Table S6).

Table S6. Spectrophotometric Analyses of Free Amine on the Tripod

Au-tripod-x (x = MW)	Coverage (PEG/NP)		Footprint (nm^2)*	
	Coupling-Cleavage Method	Fluorescamine method	Coupling-Cleavage Method	Fluorescamine method
Au-tripod-2000	938 ± 82	1279 ± 151	0.835 ± 0.073	0.613 ± 0.072
Au-tripod-3400	757 ± 56	1028 ± 126	1.035 ± 0.076	0.762 ± 0.093
Au-tripod-6000	577 ± 25	633 ± 74	1.358 ± 0.059	1.238 ± 0.143

* The total surface area of ideal tripods = 783.6 nm^2, according to the size and shape of tripods.

Fluorescamine method. A 10 µl aliquot of 0.2 M of aqueous potassium cyinide (KCN) was added to oxidatively etch the tripods (60 µl of 5 nM) and release the attached monolayer PEG. The resultant solution was incubated at room temperature for 30 min until the disappearance of the tripods plasmon resonance absorption band at ca. 520 nm and 700 nm. Seventy microliter of water and 50 µl of 100 mM borate buffer were then added to the above mixture. The resultant mixture was added 10 µl of fluorescamine solution in acetonitrile, and incubated for 20 min in the dark at room temperature. fluorescence spectra and intensities were recorded on a TECAN Infinite M1000 microplate reader (TECAN Group Ltd.). Excitation wavelength was set at 395 nm, and the emission wavelength was set at 480 nm. The spectral measurement was done in tetraplicate. A linear absorption versus concentration calibration curve was constructed by adding known amounts of butylamine in water to the reaction solution under the same condition described above.

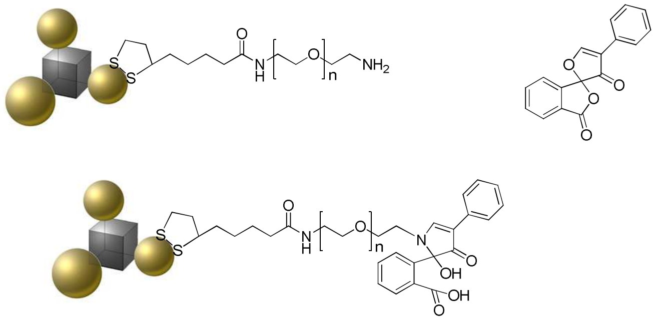

Figure S24. Fluorescent quantification of amino groups on tripods.

6. Size, Zeta Potential and stability test of functionalized Au-tripods.

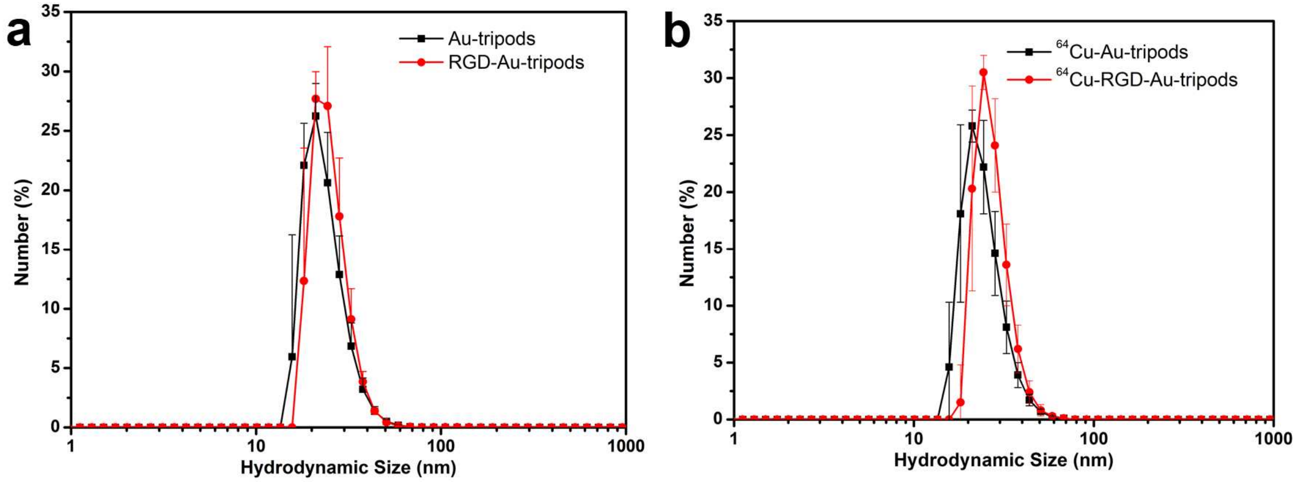

Figure S25. Hydrodynamic size of (A) Au-tripods and RGD-Au-tripods, (B) ^{64}Cu-Au-tripods and ^{64}Cu-RGD-Au-tripods.

Table S7. Hydrodynamic Size of Functionalized Au-tripods.

NPs	Hydrodynamic size (nm)	NPs	Hydrodynamic size (nm)
Au-tripods	20.6 ± 0.5	^{64}Cu-Au-tripods	21.2 ± 0.6

RGD-Au-tripods	22.8 ± 0.6	^{64}Cu-RGD-Au-tripods	24.1 ± 0.8

Table S8. Zeta Potentials of Functionalized Au-tripods.

NPs	Zeta Potential (mV)	NPs	Zeta Potential (mV)
Au-tripods	24.6 ± 0.5	^{64}Cu-Au-tripods	23.1 ± 1.0
RGD-Au-tripods	-18.6 ± 0.8	^{64}Cu-RGD-Au-tripods	-21.3 ± 1.1

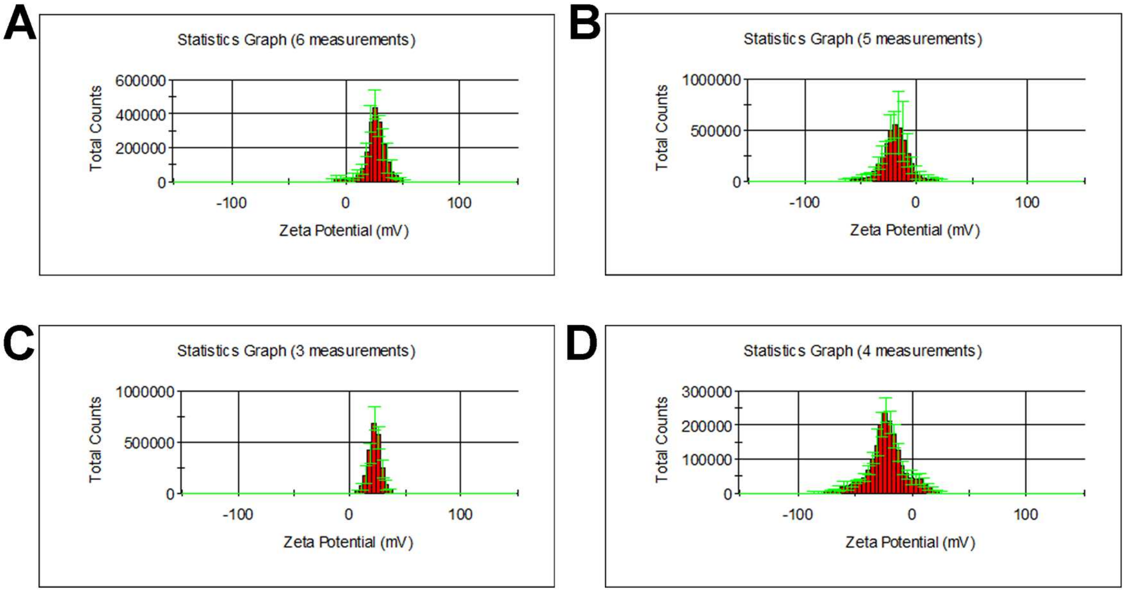

Figure S26. Zeta potential statistics graphs of various tripods: (A) Au-tripods, (B) RGD-Au-tripods. (C) ^{64}Cu-Au-tripods, (D) ^{64}Cu-RGD-Au-tripods.

Stability of the hydrodynamic size during serum incubation. The stability of RGD-Au-tripods in serum was validated by measuring the hydrodynamic size distribution of RGD-Au-tripods using DLS. The RGD-Au-tripods were added to 10% fetal bovine serum (FBS) in PBS at a concentration of 2 nM and incubated at 37°C upto 24 hours. The aliquots were analyzed at 0, 4, 8, 24, and 48 h post-incubation by DLS. The average sizes of RGD-Au-tripods remained same over the course of 48 hour incubation, indicating that the RGD-Au-tripods are stable in physiological condition.

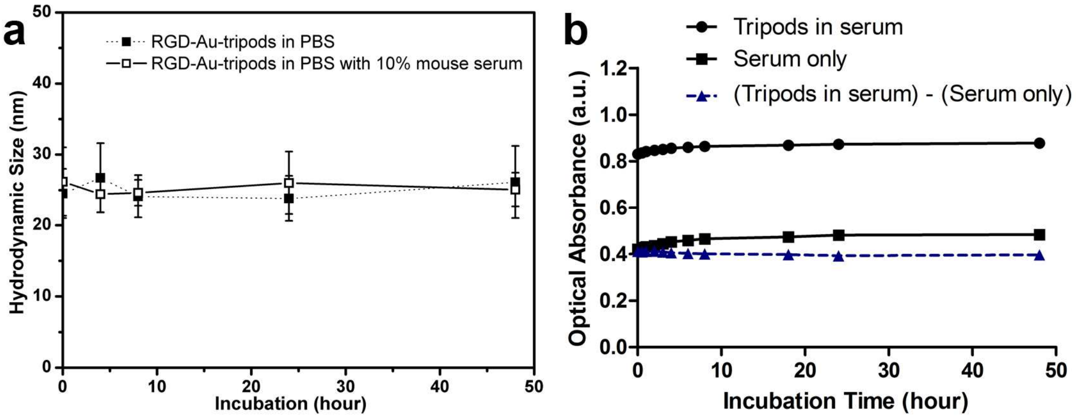

Figure S27. Stability Test of RGD-Au-tripods. (a) Stability of the hydrodynamic size during serum incubation. (b) Optical serum stability of Au-triopds.

Serum stability of the photoacoustic signal. To verify the stability of the optical absorbance and photoacoustic signal of Au-tripods in serum, we suspended the Au-tripods in 50% mouse serum/50% PBS (total volume 1 mL, concentration of tripods = 500 pM, *n* = 3). We monitored the optical absorbance of the Au-tripod solution at 700 nm at multiple time points for 48 h (Figure S25b). We noticed a slight increase in the optical absorbance of the control serum vial over 48 hours, probably due to the slight evaporation of water from the vials. The same effect could be observed in the vials containing the Au-tripods in serum. After concentration correction (subtracting the serum only absorbance from Au-tripods in serum), the optical absorbance of tripods show a stable and consistent absorbance curve over 48 hours with a standard deviation from the mean average absorbance of 5%.

7. Quantification Analysis of number of NOTA groups on NOTA- RGD-Au-tripods.

The average number of NOTA chelators on each NOTA-RGD-Au-tripods was measured using a modified procedure.[17,18] Briefly, 100 µCi of $^{64}CuCl_2$ in 10 µl of 100 mM 0.1 M sodium acetate buffer (pH = 5.0), used as an internal reference, was added into a known amount of non-radioactive $CuCl_2$ in sodium acetate buffer (mole$_{Cu}$, 200 fold excess of tripod concentration, 50 µl of 20 µM). Five picomolars of NOTA-RGD-Au-tripods in 50 µl of sodium acetate buffer were added to the above solution. The resultant mixture was incubated at 40°C for 1 hour with constant shaking. The Cu-chelated NOTA-RGD-Au-tripods (^{64}Cu-RGD-Au-tripods) were then purified using a centrifugal filter (Amicon centrifugal filter device, MWCO = 30 kDa). The decay-corrected radio-activities of both collected filtrate and filtered tripods were measured to calculate the radio-labeling yield (Y_1). Without addition of non-radioactive $CuCl_2$, the yield (Y_0) of radio-labeling reaction was obtained at the similar condition. The moles of NOTA groups were calculated according to the following equation:

$$\text{moles of NOTA} = \text{mole}_{Cu} \times (Y_0 \times Y_1) / (Y_0 - Y_1)$$

where the mole_{cu} is the moles of non-radioactive Cu, and Y_0 is the yield of radio-labeling reaction without addition of non-radioactive Cu, and Y_1 is the radio-labeling yield while a known amount of non-radioactive Cu is added. The average number of NOTA groups on RGD-Au-tripods was determined as ratio of the moles of NOTA groups to moles of tripods. Typically, the average number of NOTA per tripod equals 54.5 ± 3.3 (n = 3). Assuming one hundred percentage yield of conjugating RGD on the rest of amino groups (See section of Quantification of PEG density on PEGylated Au-tripods) via crosslinkers, the ratio of RGD to NOTA on tripods was 12.89:1. The conjugated RGD was actually determined by measuring the differences in concentration of RGD using HPLC before and after addition of Au-tripods during the coupling reaction. The eluent from the MWCO filter was measured by integrating the area of the RGD peak in HPLC. The actual ratio of RGD to NOTA on a single tripod was 8.2:1.

8. Cellular internalization of RGD-Au-tripods.

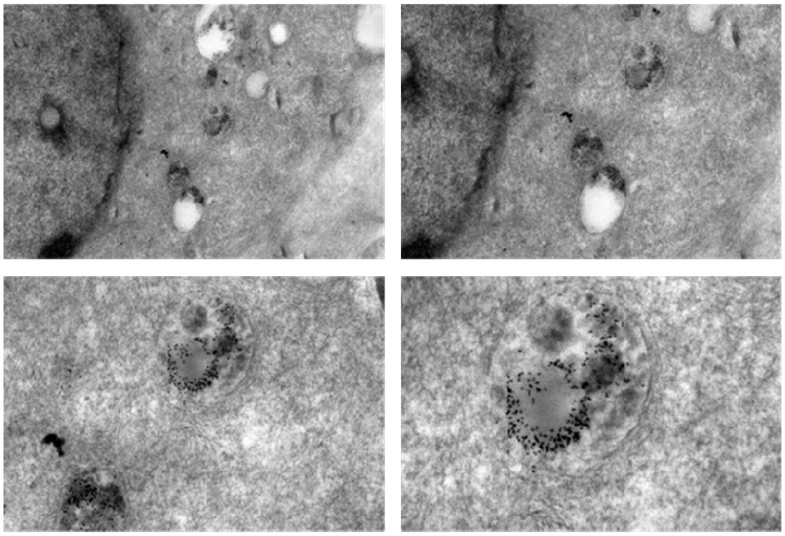

Figure S28. Internalization of RGD-Au-Tripods in U87MG cells. TEM images of cell sections were shown.

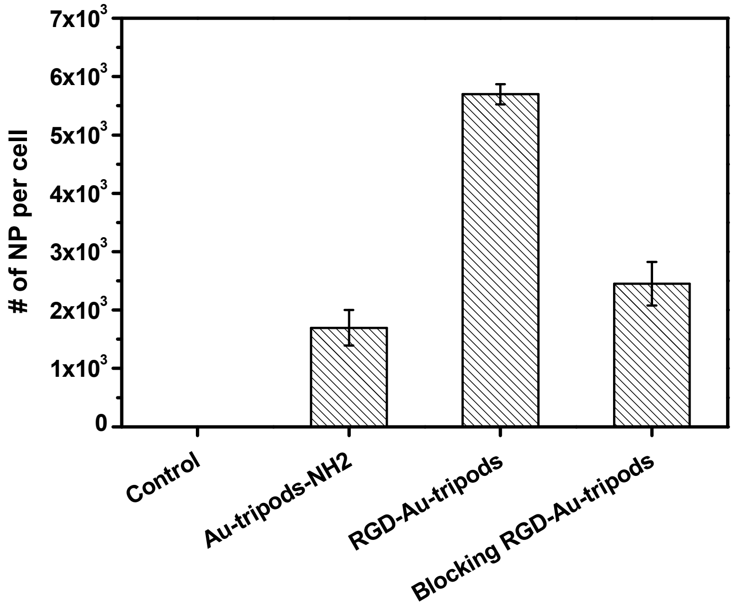

Figure S29. Cellular uptake of RGD-Au-Tripods.

9. Radio labeling and *in vivo* biodistribution and tumor targeting of Au-tripods and Au-rods

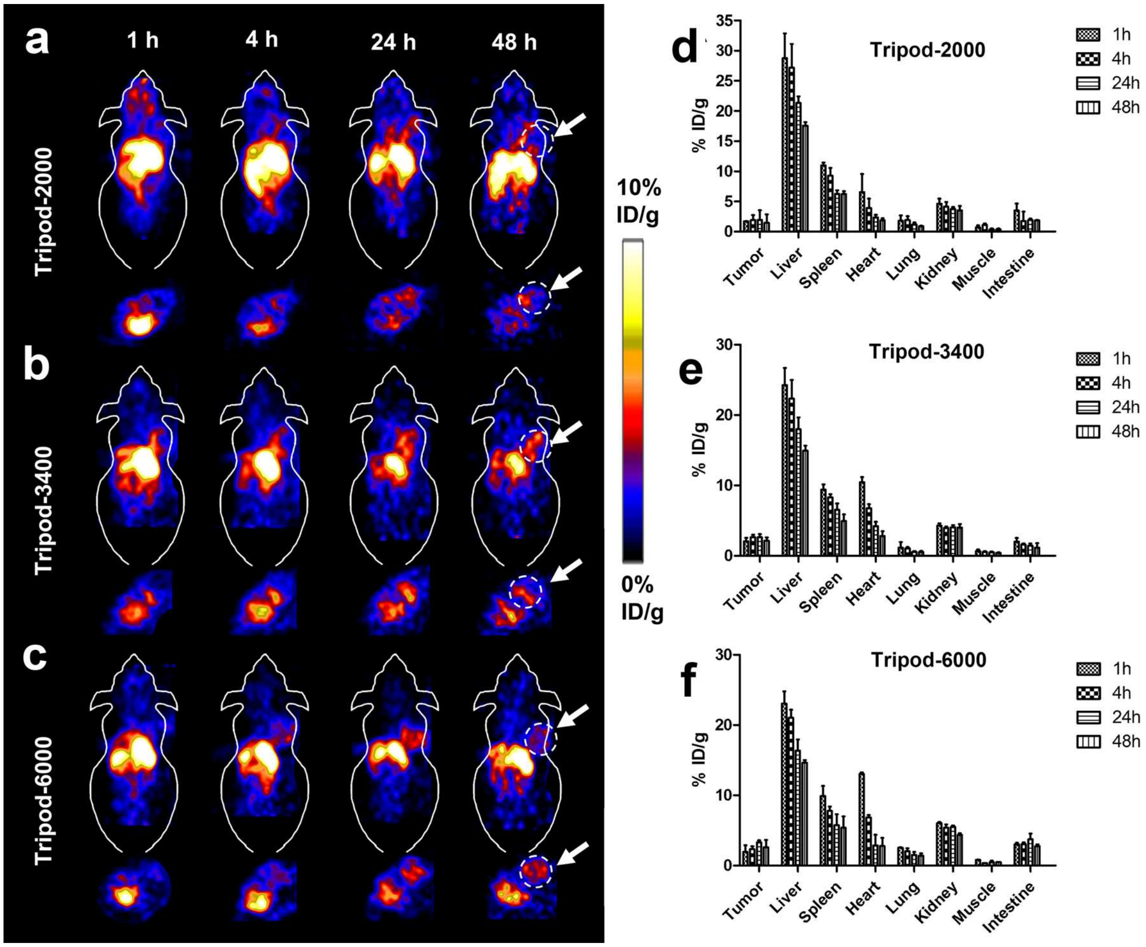

Figure S30. Small animal PET images and PET quantification of intravenous injected tripods with different surface functionalization in mice bearing the U87MG human glioblastroma tumor. **a-c**, Decay-corrected whole-body coronal PET images of nude mice bearing human U87MG tumor at 1, 4, 24, and 48 h after injection of 3.7 MBq of ^{64}Cu-Au-tripod-2000, ^{64}Cu-Au-tripod-3400, and ^{64}Cu-Au-tripod-6000 (200 pmol / kg of mouse body weight, or 2 mg / kg of mouse body weight, $n = 4$ for each group). The dashed cicles delineate the margins of tumors. The white arrows indicate the position of tumors. **d-f**, PET quantification of tumors and major organs after intravenous injection to mice bearing subcutaneous U87 glioma xenografts ($n = 4$ per group, data represent means ± standard deviations (SD)).

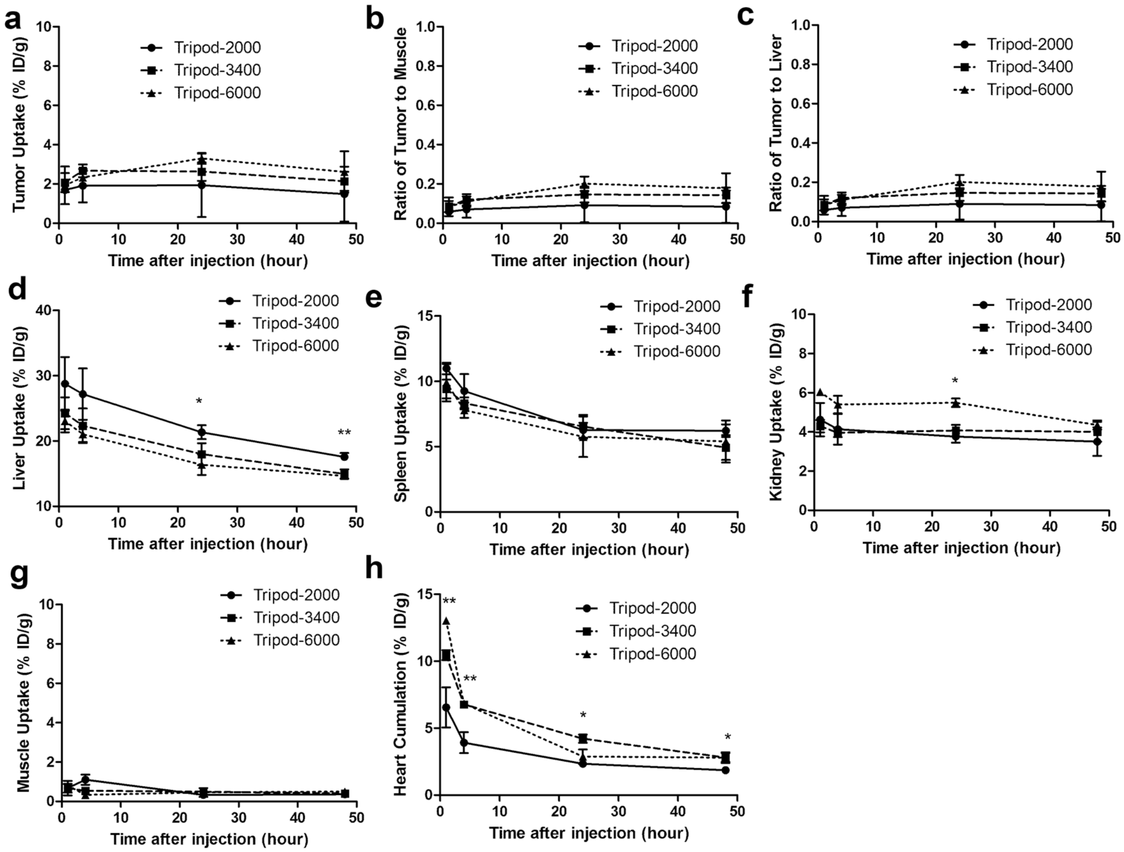

Figure S31. Comparison of tumor and major organ uptakes of three different PEGylated ^{64}Cu-Au-tripods for a time period up to 48 hours after intravenous injection to U87MG tumor-bearing mice (n = 4 per group, Data represent mean ± SD. ** $P < 0.01$, *$P<0.05$ (two-sided Student's t-test)).

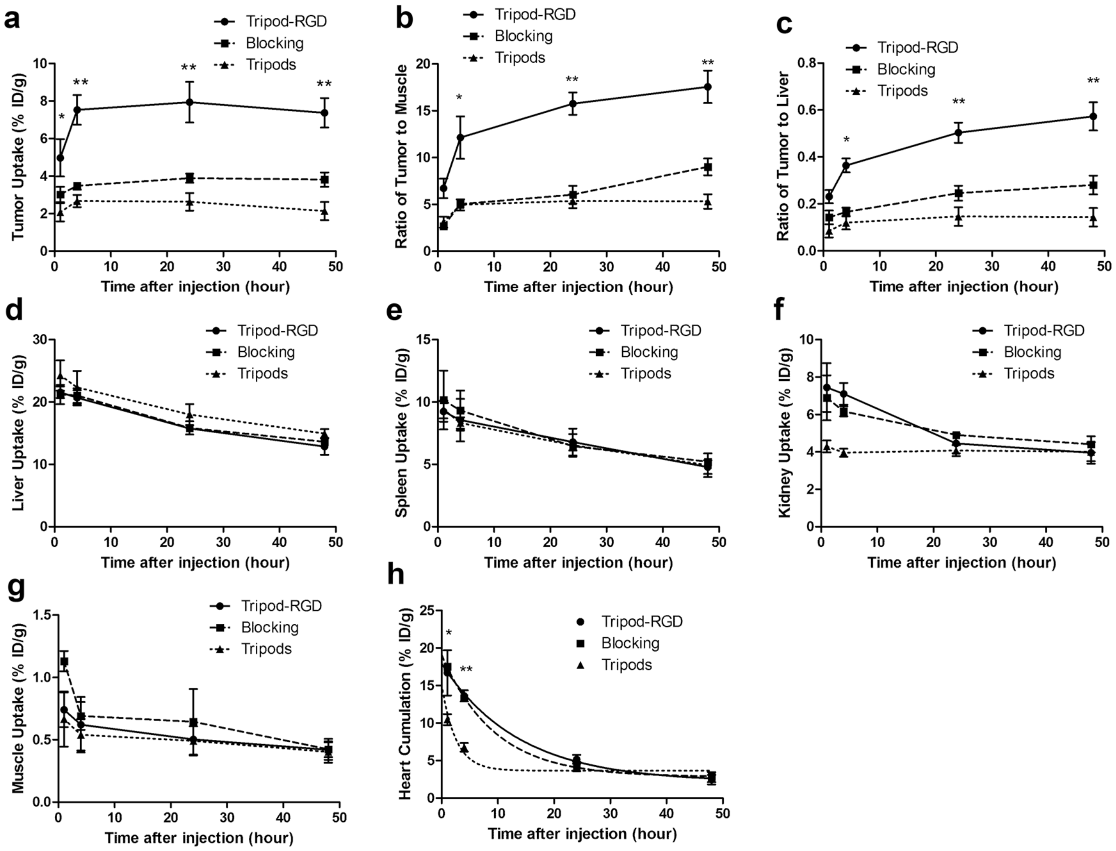

Figure S32. Comparison of tumor and major organ uptakes of ^{64}Cu-RGD-Au-tripod, ^{64}Cu-RGD-Au-tripod with a blocking dose of c(RGDfC), and ^{64}Cu-Au-tripod for a time period up to 48 hours after intravenous injection to U87MG tumor-bearing mice ($n = 4$ per group). Data represent mean ± SD. ** $P < 0.01$, *$P<0.05$ (two-sided Student's t-test).

The average tumor-to-muscle ratios at 4, 24, and 48 h after post injection were 12.1:1, 15.8:1, and 17.6:1, respectively, indicating that ^{64}Cu-RGD-Au-tripods were preferably deposited and retained in the tumor over the 48 h period.

Although the size difference between Au-tripods and RGD-Au-tripod is small (Au-tripod: 20.6 ± 0.5 vs. RGD-Au-tripod: 22.8 ± 0.6), we found that the zeta potential of tripods dramatically decreased from +23 mV to -21 mV upon the conjugation of RGD, The negative surface charges could significantly lower the nonspecific RES uptake and elongate the blood circulation time.

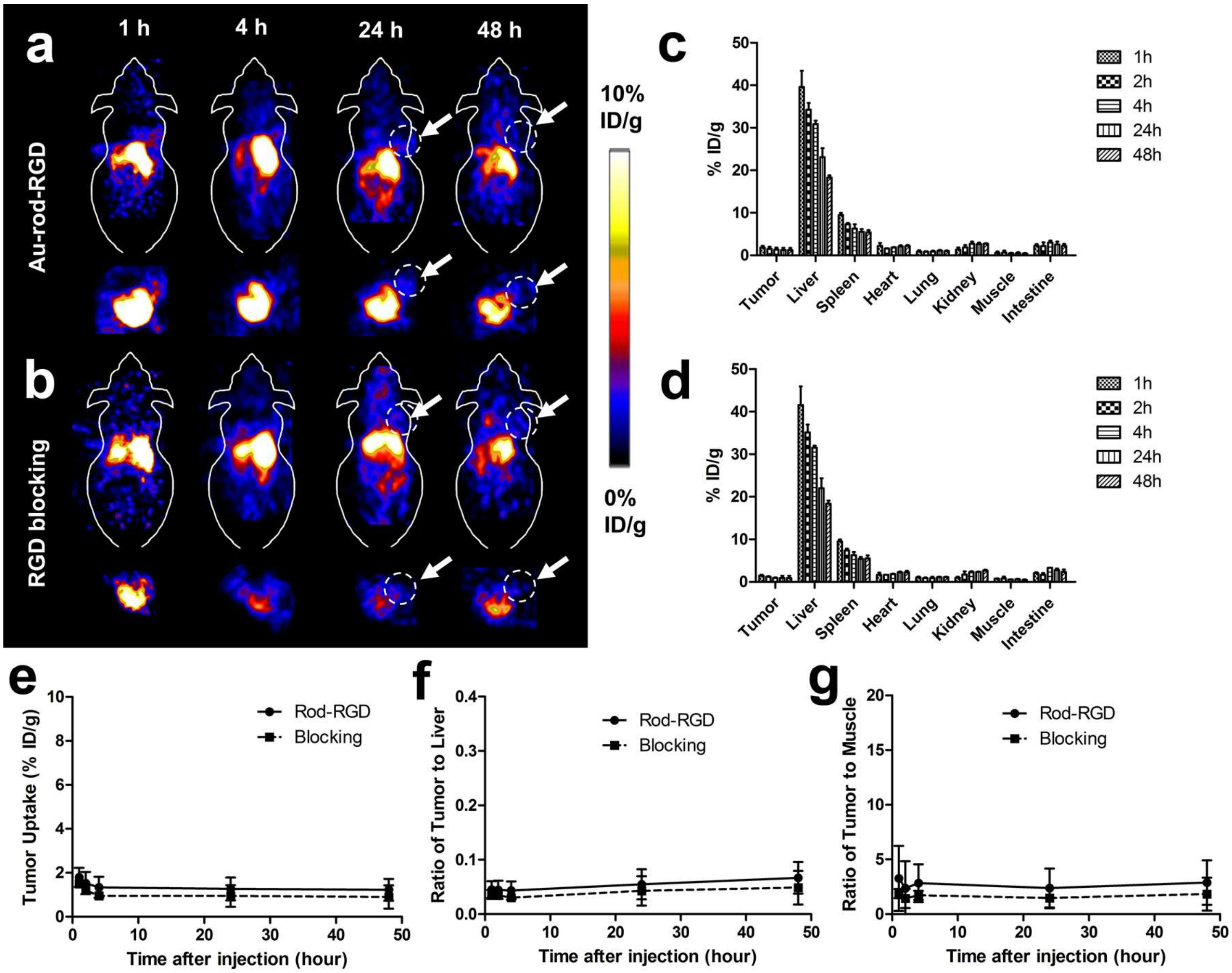

Figure S33. Small animal PET images and PET quantification of intravenous injected gold rods modified with RGD in mice bearing the U87MG human glioblastoma tumor. **a-b**, Decay-corrected whole-body coronal PET images of nude mice bearing human U87MG tumor at 1, 4, 24, and 48 h after injection of 3.7 MBq of ^{64}Cu-RGD-Au-rods (2 mg / kg of mouse body weight, *n* = 4 for each group), and ^{64}Cu-RGD-Au-rods with a blocking dose of c(RGDfC) (21 μmol of c(RGDfC)/kg of mouse body weight). The dashed cicles delineate the margins of tumors. The white arrows indicate the position of tumors. **c-d**, PET quantification of tumors and major organs after intravenous injection to mice bearing subcutaneous U87 glioma xenografts (*n* = 4 per group, data represent means ± standard deviations (SD)). **e-g**, Comparison of tumor and major organ uptakes (liver and muscle) of ^{64}Cu-RGD-Au-rods, and ^{64}Cu-RGD-Au-rods with a blocking dose of c(RGDfC) for a time period up to 48 hours after intravenous injection to U87MG tumor-bearing mice (*n* = 4 per group). Data represent mean ± SD. ** *P < 0.01, *P<0.05* (two-sided Student's *t*-test).

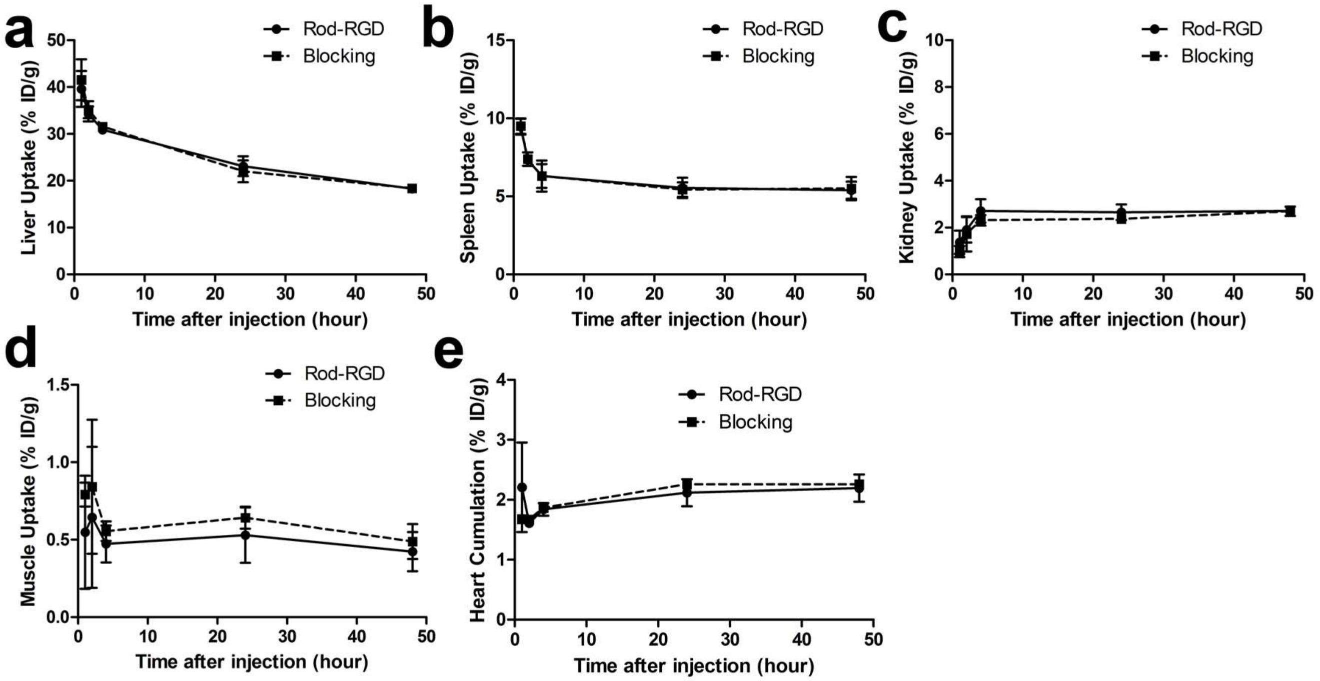

Figure S34. Comparison of tumor and major organ uptakes of ^{64}Cu-RGD-Au-rods, and ^{64}Cu-RGD-Au-rods with a blocking dose of c(RGDfC) for a time period up to 48 hours after intravenous injection to U87MG tumor-bearing mice (*n* = 4 per group). (a) liver, (b) spleen, (c) kidneys, (d) muscle, (e) heart. Data represent mean ± SD. ** *P < 0.01, *P<0.05* (two-sided Student's *t*-test).

Discussion

We had evaluated the biodistribution and specific uptake of gold rods after the tail-vein injection, and the results further confirmed that Au-tripods with controlled sizes and shapes showed improved targeting efficiency, pharmacokinetics and biodistribution (Section C.9, and Figure S33 and S34) compared to the regular gold rods. There was no significant difference in PET imaging of intergrin receptors of U87MG tumors between RGD coated Au-rods and the control sample. Their tumor uptakes of 2~3% ID/g after 24 h post-injection were much lower than that of Au-tripods at the same condition.

10. Pilot acute toxicity analysis of tripods

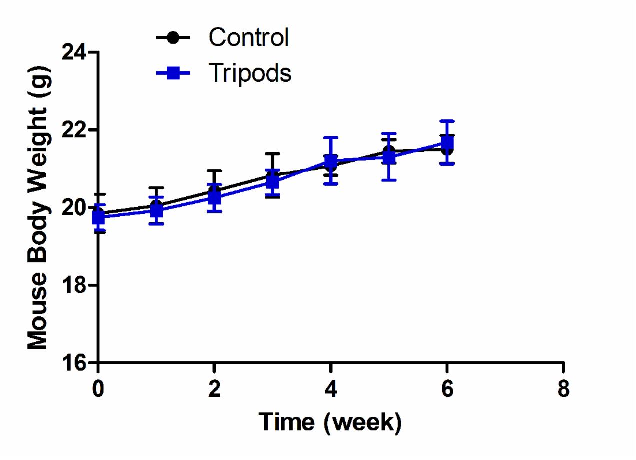

Figure S35. Change in body weight of mice injected with Au-tripods compared with PBS control (*n* = 4). There is no statistically significant difference in the mass change between control and Au-tripods injected mice over a period of 6 weeks. The error bars represent standard deviation (SD).

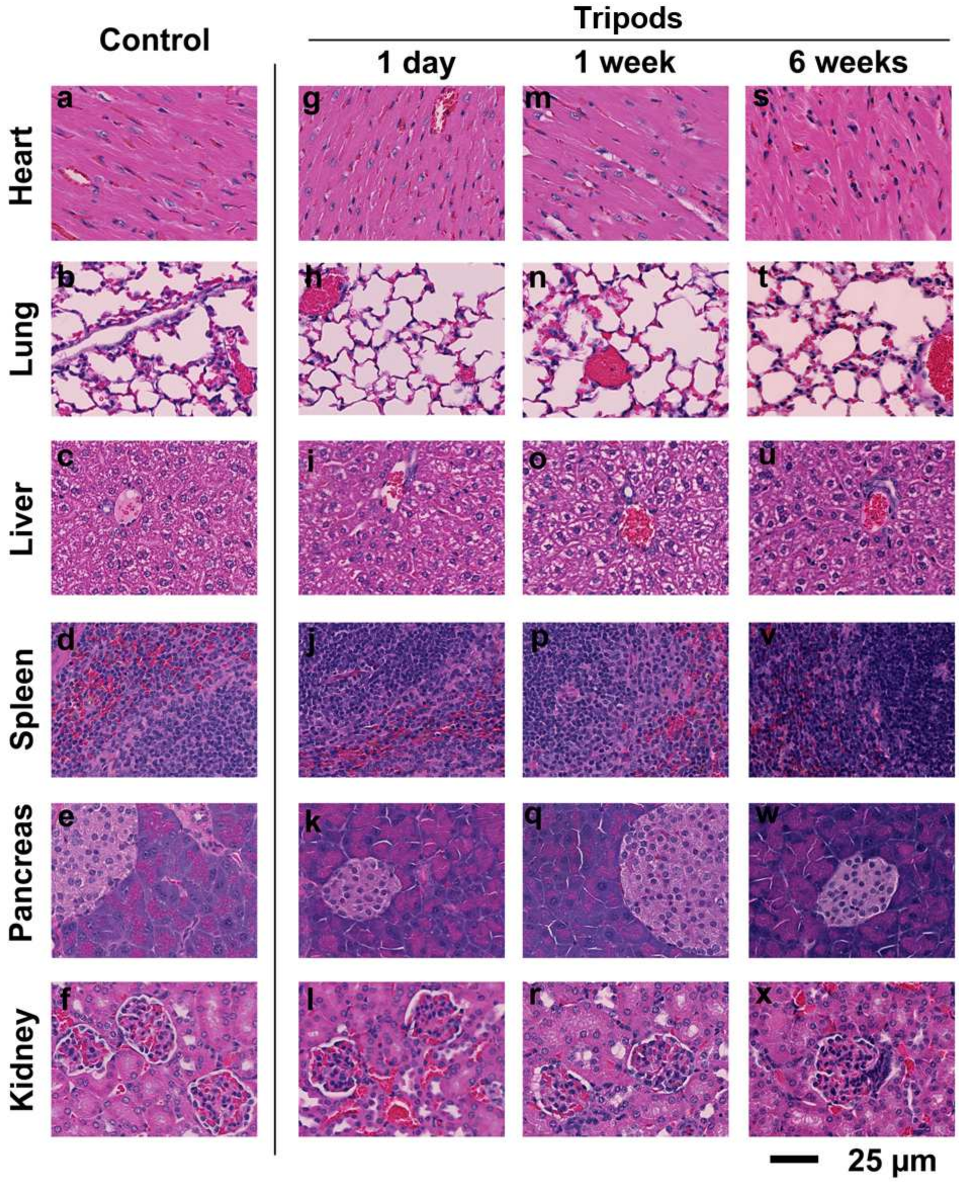

Figure S36. Histologic and microscopic examinations of major organs of Balb/C mice after being administered either PBS buffer or tripods (intravenous injection of 20 pmol Au-tripods (~200 µg of total weight based on the ICP result)). Organs were stained with heamatoxylin and eosin. Histolgic examination of the major organs (including heart, lung, liver, kidney, spleen and pancreas) failed to reveal any significant microscopic lesions in tripod treated mice (*n* = 4) over a period of 6 weeks, compared to the control group.

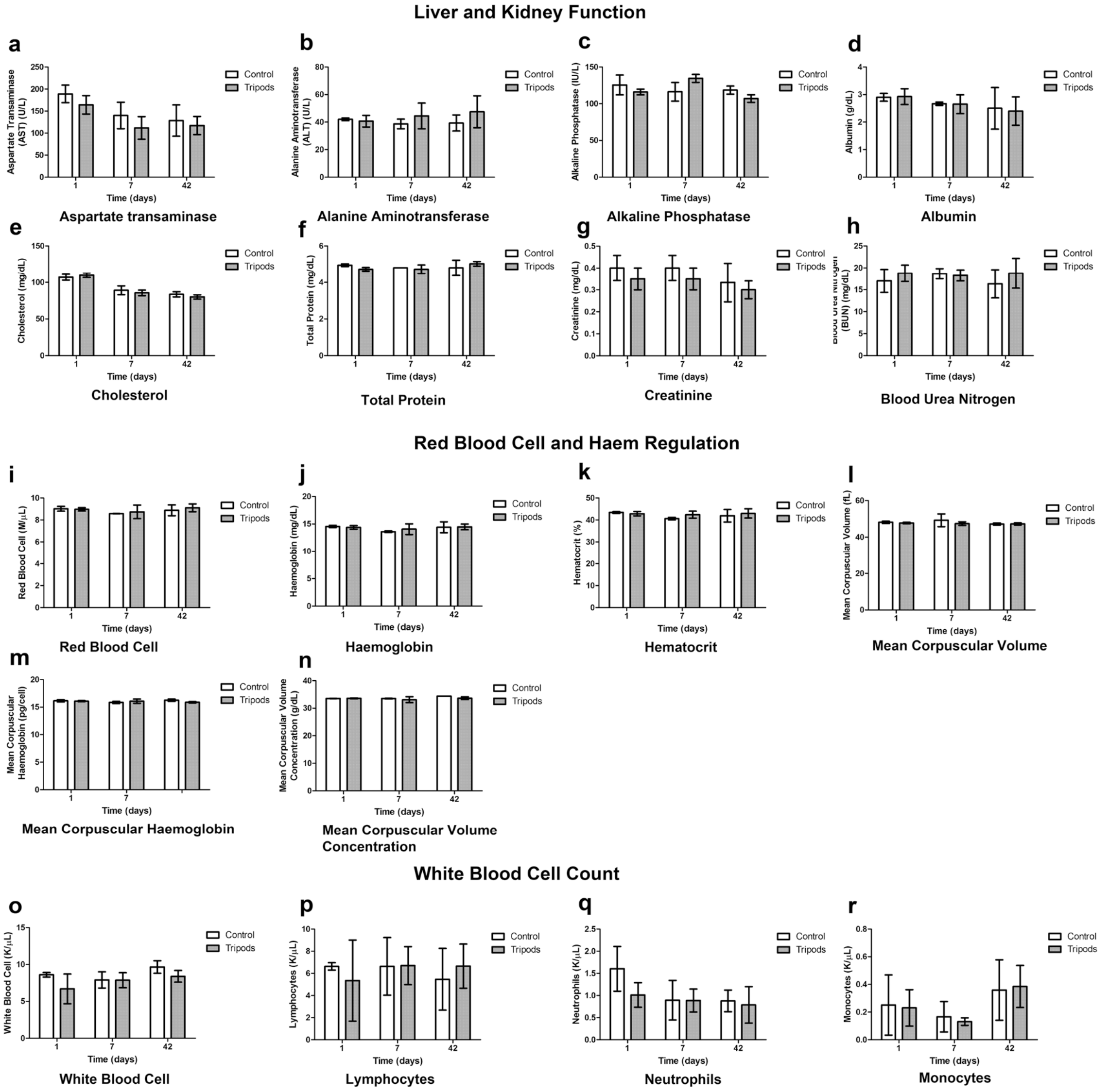

Figure S37. Blood test parameters for mice with i.v. administration of tripods (20 pmol) and PBS (mean ± SD, *n* = 4). Hematology results showed the parameters (I) of liver and kidney function: (**a**) aspartate transaminase, (**b**) alanine aminotransferase (ALT), (**c**) alkaline phosphatase, (**d**) albumin, (**e**) cholesterol, (**f**) total protein, (**g**) creatinine, (**h**) blood urea nitrogen; the parameters (**II**) of red blood cell and haem regulation: (**i**) red blood cell, (**j**) haemoglobin, (**k**) haematocrit, (**l**) mean corpuscular volume, (**m**) mean corpuscular haemoglobin, (**n**) mean corpuscular volume concentration; and the parameters (**III**) of white blood cell count: (**o**) white blood cell, (**p**) lymphocytes, (**q**) neutrophils, (**r**) monocytes. Comparing each sample group to the related control group, these blood test parameters did not indicate a trend in toxicity of Au-tripods. The error bars represent standard deviation (SD), *n* = 4.

In order to obtain a better understanding of the *in vivo* behavior of Au-tripods and study their potential toxicity, we carried out a pilot study to assess the potential toxicity of tripods. The mice were treated with a high dose of tripods (20 pmol PEGylated Au-tripod or 8 mg per kg mouse).[13] Mice were carefully monitored throughout the study, and remained healthy over a six-week period, as demonstrated by a lack of major behavior changes, including their body weight loss, physical appearance, behavior and interactions toward other animals (Supporting Information Figure S30). At each time point after injection (1 day, 1 week, and 6 weeks), four mice per group were euthanized and blood was collected immediately for hematology analysis and serum biochemistry analysis. Necropsies were performed for gross pathologic evaluation and collection of major organs and tissues (heart, lungs, brain, kidneys, liver, spleen and pancreas). Liver and kidney function tests indicated that the hepatic and renal function of the mice were normal (Supporting Information Figure S32). Red blood cell counts and attributes were unaffected by the large dose of tripods. Unaffected white blood cell counts revealed that tripods were not immunogenic in the six-week time period. Histologic and microscopic examination revealed there were no common or uncommon toxic changes in the major parenchymal organs examined (Supporting Information Figure S31). Although this was a pilot toxicity study, the systematic toxicity evaluation suggested that tripods are likely highly biocompatible in small living subjects.

11. in vitro and in vivo PAI

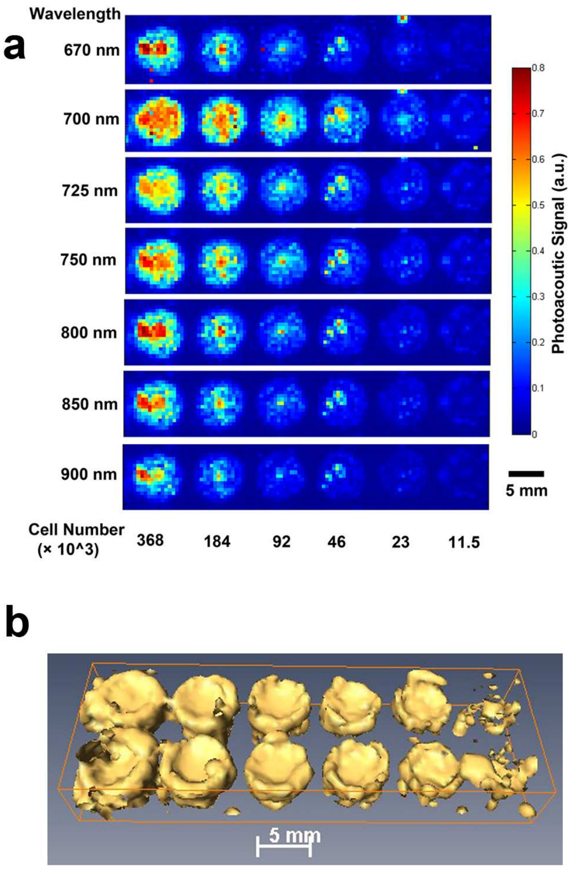

Figure S38. **a**, Maximum intensity projection photoacoustic images of the same agarose phantom. The color bar at the right represent relative photoacoustic signal intensity. **b**, A 3D rendering of photoacoustic images of tripod-stained cells.

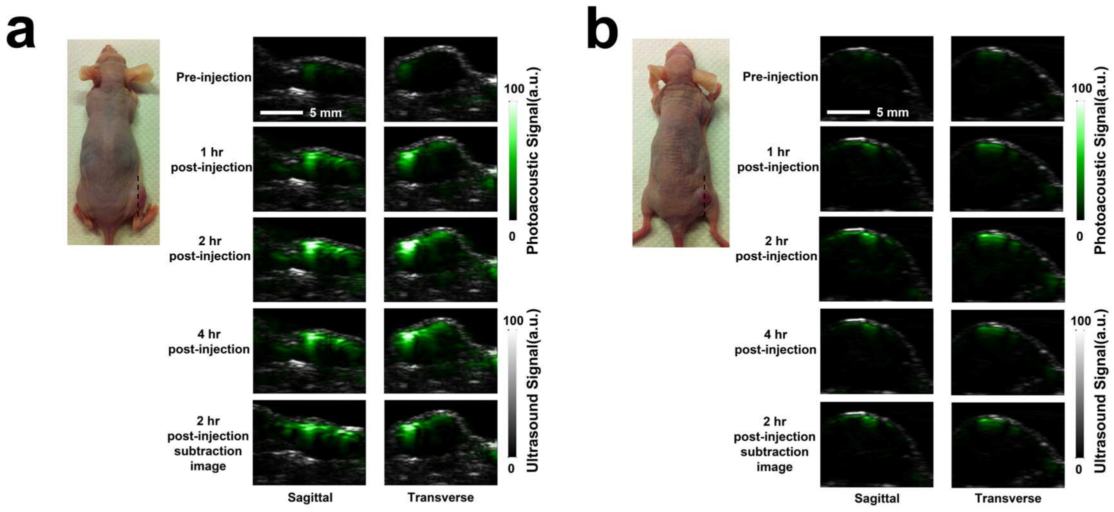

Figure S39. Targeting of integrin $\alpha_v\beta_3$-postitive U87MG tumor in mice by RGD-Au-tripod. a and **b**, Photographs of the tumors in mice and corresponding ultrasound (gray) and photoacoustic (green) images of two vertical slices through the tumor (sagittal and transverse views). The ultrasound images show the skin and the tumor boundaries.

12. Histologic and microscopic examination

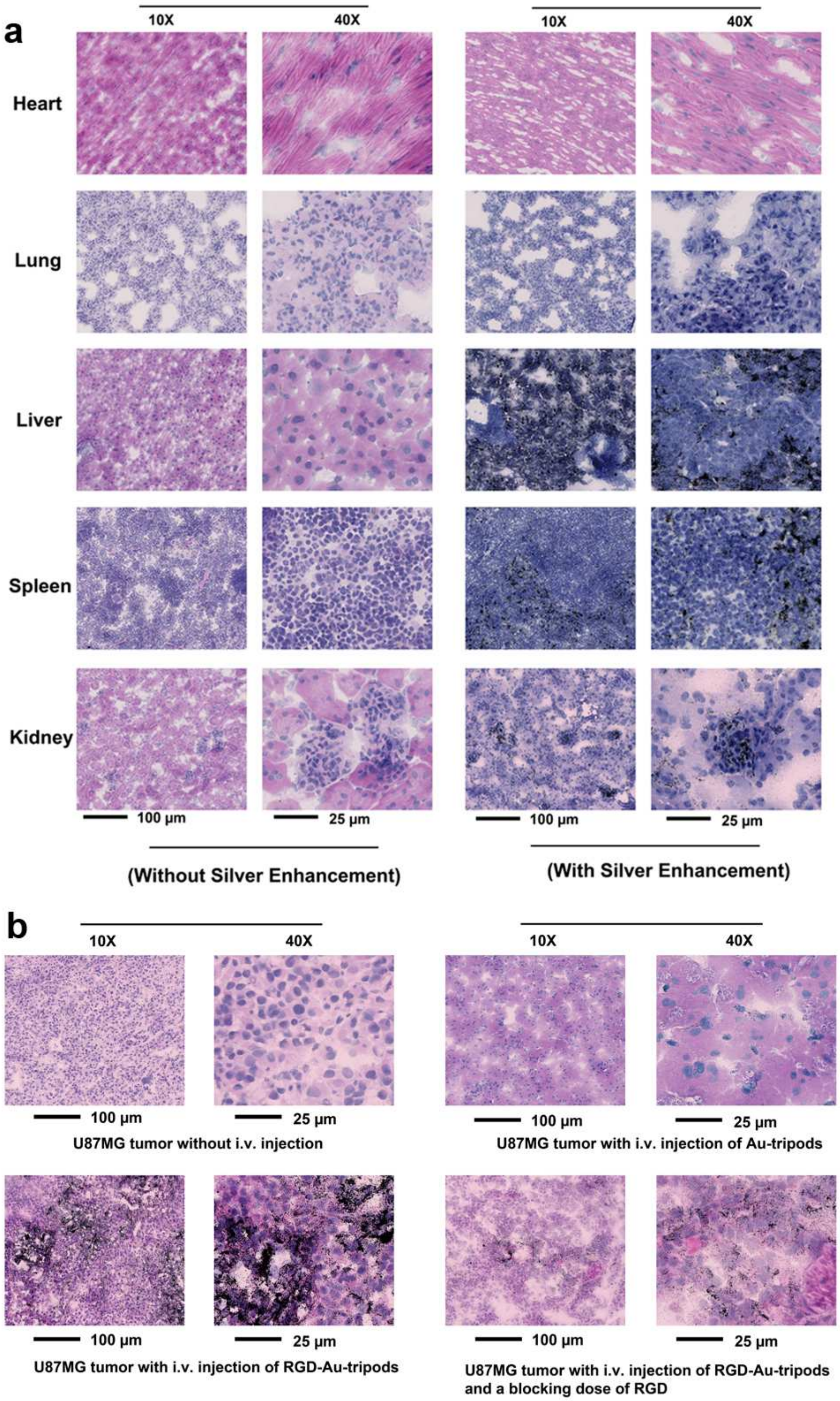

Figure S40. Representative light micrographs of tumor and major organ sections of nude mouse bearing U87MG tumor 24 hours after being administered tripods with or without silver-enhancement. **a**, The major organs (e.g., heart, lung, liver, spleen, pancreas, and kidney) were stained with heamatoxylin and eosin and did not exhibit any significant microscopic lesions (left columns). The silver enhanced sections of major organs displayed the most intense staining in the liver, spleen and kidney. Right column illustrated that magnified organ sections with silver enhancement (black dots). **b**, Histologic examination of tumor sections from control mice and tumor-bearing mice treated with tripod, tripod-RGD, and RGD-Au-tripods with a blocking dose of c(RGDfC).

References for Supporting Information

(1) Liu, W.; Howarth, M.; Greytak, A. B.; Zheng, Y.; Nocera, D. G.; Ting, A. Y.; Bawendi, M. G. *Journal of the American Chemical Society* **2008**, *130*, 1274.

(2) Zalipsky, S.; Gilon, C.; Zilkha, A. *Eur Polym J* **1983**, *19*, 1177.

(3) Nikoobakht, B.; El-Sayed, M. A. *Chemistry of Materials* **2003**, *15*, 1957.

(4) Cheng, Z.; De Jesus, O. P.; Kramer, D. J.; De, A.; Webster, J. M.; Gheysens, O.; Levi, J.; Namavari, M.; Wang, S.; Park, J. M.; Zhang, R.; Liu, H.; Lee, B.; Syud, F. A.; Gambhir, S. S. *Molecular Imaging and Biology* **2010**, *12*, 316.

(5) Cheng, K.; Peng, S.; Xu, C. J.; Sun, S. H. *J Am Chem Soc* **2009**, *131*, 10637.

(6) Miao, Z.; Ren, G.; Liu, H.; Jiang, L.; Cheng, Z. *J Biomed Opt* **2010**, *15*, 036007.

(7) Miao, Z.; Ren, G.; Liu, H.; Jiang, L.; Cheng, Z. *Bioconjug Chem* **2010**, *21*, 947.

(8) Knoess, C.; Siegel, S.; Smith, A.; Newport, D.; Richerzhagen, R.; Winkeler, A.; Jacobs, A.; Goble, R. N.; Graf, R.; Wienhard, K.; Heiss, W. D. *Eur J Nucl Med Mol I* **2003**, *30*, 737.

(9) de la Zerda, A.; Bodapati, S.; Teed, R.; May, S. Y.; Tabakman, S. M.; Liu, Z.; Khuri-Yakub, B. T.; Chen, X.; Dai, H.; Gambhir, S. S. *ACS Nano* **2012**, *6*, 4694.

(10) Levi, J.; Kothapalli, S. R.; Ma, T.-J.; Hartman, K.; Khuri-Yakub, B. T.; Gambhir, S. S. *J Am Chem Soc* **2010**, *132*, 11264.

(11) Kircher, M. F.; de la Zerda, A.; Jokerst, J. V.; Zavaleta, C. L.; Kempen, P. J.; Mittra, E.; Pitter, K.; Huang, R.; Campos, C.; Habte, F.; Sinclair, R.; Brennan, C. W.; Mellinghoff, I. K.; Holland, E. C.; Gambhir, S. S. *Nat Med* **2012**, *18*, 829.

(12) Loening, A.; Gambhir, S. *Molecular Imaging* **2003**, *2*, 131.

(13) Thakor, A. S.; Luong, R.; Paulmurugan, R.; Lin, F. I.; Kempen, P.; Zavaleta, C.; Chu, P.; Massoud, T. F.; Sinclair, R.; Gambhir, S. S. *Science Translational Medicine* **2011**, *3*, 79ra33.

(14) Wong, J. Y.; Kuhl, T. L.; Israelachvili, J. N.; Mullah, N.; Zalipsky, S. *Science* **1997**, *275*, 820.

(15) Hakkinen, H. *Nat Chem* **2012**, *4*, 443.

(16) Uyeda, H. T.; Medintz, I. L.; Jaiswal, J. K.; Simon, S. M.; Mattoussi, H. *J Am Chem Soc* **2005**, *127*, 3870.

(17) Meares, C. F.; McCall, M. J.; Reardan, D. T.; Goodwin, D. A.; Diamanti, C. I.; McTigue, M. *Analytical Biochemistry* **1984**, *142*, 68.

(18) Liu, Z.; Cai, W. B.; He, L. N.; Nakayama, N.; Chen, K.; Sun, X. M.; Chen, X. Y.; Dai, H. J. *Nature Nanotechnology* **2007**, *2*, 47.